

NO_x Emissions Constraints from GEMS NO₂ Retrievals: Inversion Methodology and Air Quality Model Evaluation in Bangkok using ASIA-AQ Multi-Platform Observations

Julianna A. Christopoulos¹, Pablo E. Saide^{1,2}, Manas R. Mohanty¹, Nattamon Maneenoi¹, Jhoon Kim³, Laura Judd⁴, Katherine R. Travis⁴, Savitri Garivait^{5,6}, Agapol Junpen^{5,6}, Kazuyuki Miyazaki^{7,8}, Jinkyul Choi^{7,8}, Takashi Sekiya⁹, David Peterson¹⁰, Theodore M. McHardy¹⁰, Nicholas Gapp¹¹, Jason M. St. Clair^{12,13}, Erin Delaria^{14,15}, Glenn M. Wolfe¹², Abby Sebol¹⁵, Alessandro Franchin¹⁶, Changmin Cho¹⁶, Morgan L. Silverman^{4,17}, James H. Crawford⁴

¹Department of Atmospheric and Oceanic Sciences, University of California, Los Angeles, Los Angeles, CA, USA

²Institute of the Environment and Sustainability, University of California, Los Angeles, Los Angeles, CA, USA

³Department of Atmospheric Sciences, Yonsei University, Seoul, South Korea

⁴NASA Langley Research Center, Hampton, VA, USA

⁵The Joint Graduate School of Energy and Environment, King Mongkut's University of Technology, Thonburi, Thailand

⁶Center of Excellence on Energy Technology and Environment, PERDO, Ministry of Higher Education, Science, Research and Innovation, Bangkok, Thailand

⁷Jet Propulsion Laboratory (JPL), California Institute of Technology, Pasadena, 91109 CA, USA

⁸Joint Institute for Regional System Science and Engineering (JIFRESSE), University of California, Los Angeles, Los Angeles, CA, USA

⁹Japan Agency for Marine-Earth Science and Technology, Yokohama, Japan

¹⁰U.S. Naval Research Laboratory, Monterey, CA, USA

¹¹Science Applications International Corporation, Monterey, CA

¹²Atmospheric Chemistry and Dynamics Laboratory, NASA Goddard Space Flight Center, Greenbelt, USA

¹³GESTAR II, University of Maryland Baltimore County, Baltimore, USA

¹⁴ESSIC, University of Maryland, College Park, USA

¹⁵Department of Atmospheric and Oceanic Science, University of Maryland, College Park, USA

¹⁶Atmospheric Chemistry Observations and Modeling Laboratory, NSF National Center for Atmospheric Research, Boulder, CO, USA

¹⁷Science Systems and Applications, Inc. Hampton, VA, USA

Correspondence to: Julianna A. Christopoulos (juliechristo@g.ucla.edu)

37 **Abstract.** Nitrogen Dioxide (NO₂) is a key component of tropospheric chemistry and air quality, yet large uncertainties persist
38 in regional NO_x emissions across rapidly developing megacities in Southeast Asia. Observations from the Geostationary
39 Emissions Monitoring Spectrometer (GEMS) provide new constraints on anthropogenic NO₂ variability, while the 2024 NASA
40 Airborne and Satellite Investigation of Asian Air Quality (ASIA-AQ) campaign, offers an extensive, independent dataset for
41 model evaluation. Here, we examine air quality in Bangkok using coarse (20 km) and high-resolution (4 km) WRF-Chem
42 simulations during ASIA-AQ. We develop a top-down framework that uses hourly GEMS NO₂ columns to derive constraints
43 on the daytime cycle of NO_x emissions. Emissions are first estimated from GEMS using a Cross-Sectional Flux (CSF) inversion
44 and then incorporated into WRF-Chem through a novel optimization that reshapes the magnitude and daytime structure of
45 NO_x while accounting for lifetime and satellite vertical sensitivity. GEMS-constrained NO_x emissions for March 2024 are
46 estimated to range from 2.7 to 4.3 kT month⁻¹ after accounting for known low biases in the GEMS retrievals. Re-running WRF-
47 Chem with the updated emissions leads to substantial improvements in modeled NO₂ magnitude and temporal variability when
48 evaluated against independent ground-based, Pandora, and airborne measurements. Remaining negative biases are consistent
49 with a systematic low bias in the GEMS v3 NO₂ product, highlighting the importance of multi-platform evaluation using
50 independent observations. Together, these results demonstrate the value of hourly geostationary observations combined with
51 high-resolution modeling as a scalable pathway for improving urban NO_x emissions estimates and air quality simulations in
52 Southeast Asia.

53 **1 Introduction**

54 The troposphere contains a variety of pollutants and aerosols that degrade air quality and affect human health (Chen and Chen,
55 2021; Fuller et al., 2022; Shetty et al., 2023). Nitrogen oxides (NO_x = NO + NO₂) are primary pollutants with significant
56 variability in space and time (Seinfeld and Pandis, 2016). Information on NO_x sources is crucial in defining its concentration
57 and distribution (Miyazaki et al., 2019). Nitrogen dioxide (NO₂) is fundamental to air quality and atmospheric chemistry, as it
58 is the primary precursor to surface ozone (O₃) and nitrate aerosols (Pörtner et al., 2022) and is independently linked to the
59 development of pediatric asthma (Anenberg et al., 2022). It is thus inherent that NO₂, and its sources, are well quantified and
60 studied to gain insights into its environmental impact.

61
62 Over the past two decades, satellite observations of tropospheric NO₂ have revealed substantial regional variability in
63 emissions, particularly over industrial and urban areas (Goldberg et al., 2024; Park et al., 2025; Rey-Pommier et al., 2025).
64 While strict air quality policies in North America and Europe have resulted in significant NO₂ reductions, many developing
65 regions, especially the megacities of Southeast Asia, have seen increases (Elguindi et al., 2020; Georgoulias et al., 2019;
66 Miyazaki et al., 2017; Park et al., 2025; Sicard et al., 2023). Thailand, for example, has undergone rapid industrialization,
67 urbanization, and economic growth over the past 30 years, with most of this development occurring in the Bangkok
68 Metropolitan Region (BMR) (Thailand Office of the National Economic and Social Development Board, World Bank, 2017)

69 (Uttamang et al., 2018). This has led to increased emissions from vehicular traffic and industrial activity, resulting in a
70 sustained degradation of air quality (Uttamang et al., 2018). Since the mid 1990s, the BMR has frequently exceeded Thailand's
71 National Ambient Air Quality Standards (NAAQS) for particulate matter (PM) ($25 \mu\text{g m}^{-3}$) and O_3 (100 ppb), particularly
72 during the dry season (February-May) (Kumar et al., 2012; Uttamang et al., 2018, 2020, 2023). Within the BMR, there have
73 been initiatives to reduce health impacts and exposure related to $\text{PM}_{2.5}$. For example, the National Agenda Action Plan on
74 "Solving the Pollution Problems of Particulate Matter" motivated implementation measures in transport, industry, and waste
75 sectors (Aung et al., 2025). However, achieving the air quality standard has remained an issue. Modeling studies have shown
76 that O_3 levels typically peak between January and March, coinciding with increased solar radiation, higher temperatures,
77 elevated humidity, and prevailing northeasterly winds during the Northeast monsoon season. These meteorological conditions,
78 combined with rising emissions, often contribute to O_3 pollution episodes in the region (Uttamang et al., 2020). A key limitation
79 of these air quality modeling studies is the uncertainty in bottom-up anthropogenic emissions inventories, which remain a
80 significant source of error. In the BMR, uncertainties in regional emissions can be as large as a factor of 2 or higher (Bond et
81 al., 2004, 2007; Smith et al., 2011; Uttamang et al., 2020). These emissions uncertainties limit our ability to accurately simulate
82 pollutant concentrations and assess the effectiveness of emission control strategies. Thus, to address this issue, new
83 observational capabilities that can directly capture emission variability at fine spatial ($< 10 \text{ km}$) and temporal (hourly) scales
84 are needed.

85
86 We are currently entering a new era of satellite atmospheric composition monitoring with the launch of three geostationary
87 (GEO) imaging spectrometers covering a large component of the Northern Hemisphere. The Geostationary Environmental
88 Monitoring Spectrometer, GEMS (Kim et al., 2020), Tropospheric Emissions: Monitoring of Pollution, TEMPO (Zoogman et
89 al., 2017), and Sentinel-4 (Gulde et al., 2017), now provide unprecedented spatial and temporal resolution of atmospheric
90 constituents. These instruments offer hourly observations that resolve daytime variability of key pollutants, including NO_2 .
91 Until now, most studies of top-down NO_x emissions have relied on once-daily measurements from low Earth orbit (LEO)
92 satellites (i.e., OMI, TROPOMI) requiring assumptions about diurnal emission and chemistry patterns that introduce
93 uncertainties when coupled with chemical transport models, particularly those arising from coarse spatial resolution ($> 20 \text{ km}$),
94 emissions inventories, and chemical mechanisms (Park et al., 2025). Although these measurements have been invaluable for
95 global and long-term NO_x assessments, they cannot fully capture the pronounced sub-daily variability in NO_2 driven by
96 emissions, chemistry, and transport. GEO satellites now provide the capability to directly observe this hourly variability (Park
97 et al., 2025). For example, using 12 km WRF-Chem simulations Hsu et al. (2026) showed that TEMPO-derived top-down NO_x
98 emissions are broadly consistent with TROPOMI and bottom-up inventories, but noted coarse model resolution (e.g., 12 km)
99 can limit the representation of coastal meteorology and chemical nonlinearity.

100

101 GEMS was the first UV-visible hyper-spectrometer in geostationary orbit and was launched on GEO-KOMPSAT-2B on
102 February 18, 2020. GEMS measurements allow the observation of air quality constituents (e.g., NO_2 , SO_2 , O_3 , HCHO,

103 CHOCHO, and aerosols) at a spatial resolution of $3.5 \times 7.7 \text{ km}^2$ at the center of its field of regard and was the first space-based
104 instrument to provide hourly observations of these species. The GEMS field of regard covers 20 countries in Asia, E-W from
105 Japan to India, and N-S from Mongolia to Indonesia (Kim et al., 2020; Park et al., 2025). Recent work has demonstrated the
106 potential of GEMS and air quality models to estimate top-down NO_x emissions over major Asian cities during the summertime
107 (de Foy and Schauer, 2022; Park et al., 2024, 2025). These studies highlight the need for comprehensive validation involving
108 independent observations. The Airborne and Satellite Investigation of Asian Air Quality, ASIA-AQ, has provided an excellent
109 opportunity to conduct extensive validation of air pollutants across multiple Asian megacities, including Bangkok (ASIA-AQ
110 White Paper | ASIA-AQ, 2025).

111
112 In this manuscript, we aim to address these gaps specifically near Bangkok, Thailand by deriving emissions and examining
113 fine- (4 km) and coarse- (20 km) resolution Weather Research and Forecasting model coupled with Chemistry (WRF-Chem)
114 simulations driven by them during mid-March 2024. First, we derive daytime hourly NO_x emissions from GEMS over the
115 BMR in March 2024. Next, we use the GEMS emissions to constrain hourly model emissions through a novel optimization
116 technique. To conclude, we assess model performance using GEMS and independently with ground-monitor information,
117 Pandora site measurements, and airborne measurements collected during the ASIA-AQ campaign.

118

119 **2 Model configuration and experimental design**

120 To simulate air quality over the BMR, we use a regional simulation of WRF-Chem v4.2.2 in a research configuration (Table
121 1; Fig. 1) (Agarwal et al., 2024; Anav et al., 2024; Gao and Zhou, 2024; Skamarock et al., 2019). The model setup follows
122 previous WRF-Chem implementations in the Korea-United States Air Quality field study (KORUS-AQ) for air quality studies
123 over the Seoul Metropolitan Area (Choi et al., 2020; Goldberg et al., 2019; Lennartson et al., 2018; Park et al., 2021; Saide et
124 al., 2020). The model was driven by reanalysis meteorology, NCEP Final Reanalysis (NCEP FNL) (, and Copernicus
125 Modeling Service (CAM5) chemical boundary conditions (Commerce, 2000; Inness et al., 2019). Meteorology was
126 constrained using four-dimension data assimilation (FDDA) via grid nudging applied to model domains using the 0.25° NCEP
127 FNL reanalysis fields to improve large-scale wind representation. A two-domain approach with one-way nesting was
128 incorporated to gauge strengths between coarse- and high- resolution simulations. D01 (20 km) spans a large portion of the
129 GEMS field of regard, covering primary transboundary pollution sources (e.g., deserts in China/India, anthropogenic emissions
130 from China/India). A nested 4 km domain (D02) is centered over Bangkok (Fig. 1).

131

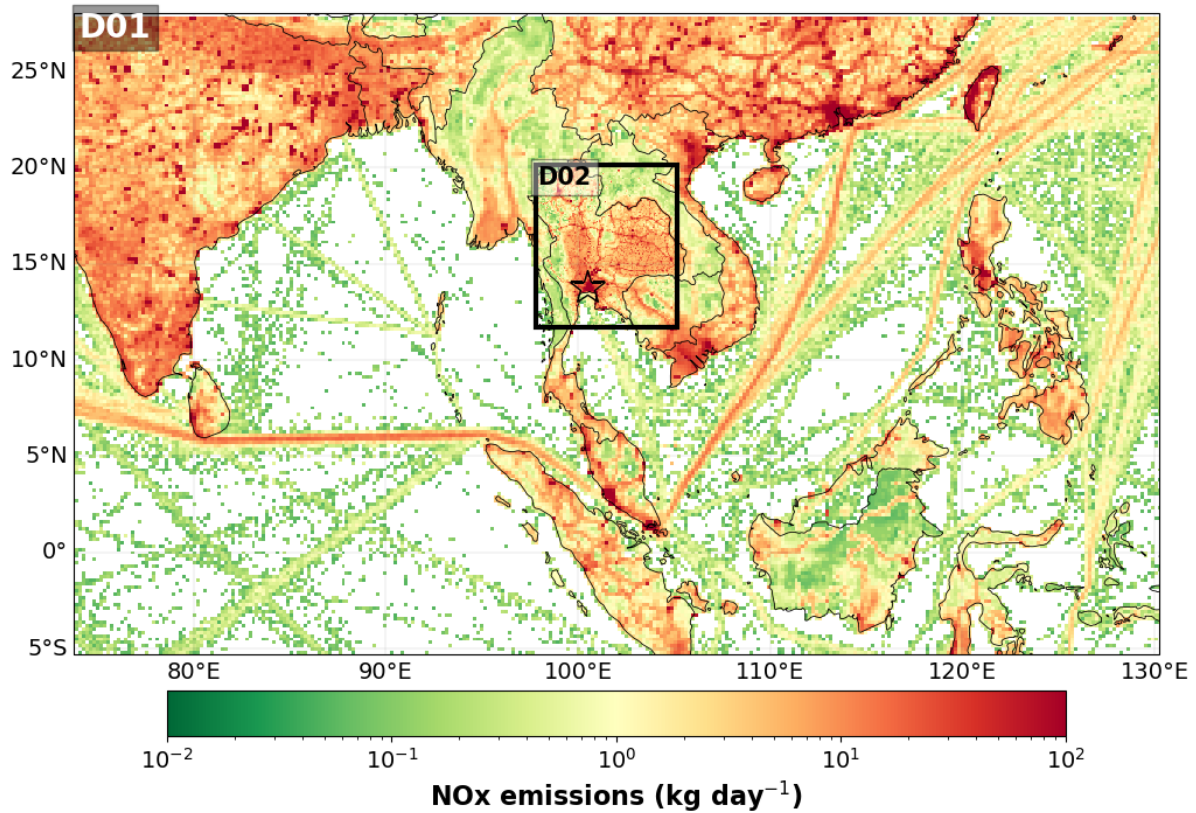
132 Original anthropogenic emissions of trace gases and primary aerosols were based on the Emissions Database for Global
133 Atmospheric Research (EDGAR v5) (Crippa et al., 2020) inventory at $0.1^\circ \times 0.1^\circ$ horizontal resolution. For D02, EDGAR
134 emissions for the transport and industrial sectors were downscaled using the Open-source Data Inventory for Anthropogenic

135 Carbon Dioxide emission inventory (ODIAC) at 1 km x 1km resolution (Oda et al., 2018). This is done by distributing EDGAR
 136 emissions into the 1 km² grid using ODIAC CO₂ as a spatial proxy in a mass conserving way. Biogenic, dust, sea salt, and fire
 137 emissions were computed within WRF-Chem using the model’s full-chemistry emission modules (Table 1). In this
 138 configuration, dust and sea-salt emissions are calculated every chemistry timestep, while biogenic emissions (MEGAN) are
 139 updated every 30 minutes. For fire emissions, plume rise is enabled, in which the injection heights are diagnosed using the
 140 plume-rise parameterization and emissions are vertically distributed (typically ~80% at the surface with the remainder aloft).
 141 The model was configured using the RACM-MADE-VBS (Ahmadov et al., 2012; Tuccella et al., 2015) chemical mechanism
 142 and physics parameterizations selected based on prior campaign experience (e.g., KORUS-AQ), with updates to better
 143 represent secondary organic aerosol formation, heterogenous chemistry, and aerosol properties. The modal aerosol scheme in
 144 MADE-VBS tracks both particle mass and number, allowing mode diameters to evolve dynamically with aerosol aging and
 145 growth processes. Hereafter, we will refer to this model configuration as WRF_{Base}. Model cases with updated anthropogenic
 146 NO_x emissions will be referred to as WRF_{Updated} and WRF_{Updated+BC} (later introduced).

147
 148 **Table 1** WRF-Chem base (WRF_{Base}) model configuration and input datasets.
 149

Component	Configuration/Source
Model Version	WRF-Chem v4.2.2
Domain	D01: 20 km (regional); D02: 4 km (nested)
Meteorological IC/BC	NCEP FNL reanalysis (0.25v x 0.25°; 6-hourly)
Chemical IC/BC	CAMS global model output
Chemistry Mechanism	RACM-MADE-VBS (with aqueous reactions)
Anthropogenic Emissions	EDGAR v5; downscaled with ODIAC CO ₂
Biogenic Emissions	MEGAN v2.1 (Guenther et al., 2006)
Biomass Burning Emissions	QFED v2.6 (Grell et al., 2011; Koster et al., 2015)
Dust Emissions	GOCART scheme (Zhao et al., 2010)
Sea Salt Emissions	Gong et al. (1997) parameterization (Gong et al., 1997)
Radiation Scheme	RRTMG (longwave); Goddard (shortwave)
Cumulus Parameterization	Grell-Freitas (D01 only)
Microphysics	Morrison (double-moment) (Ye et al., 2021)
PBL Scheme	Mellor-Yamada-Janjic TKE scheme
Simulation Period	14 – 27 March 2024

150



151

152 **Figure 1.** Spatial illustration of the WRF-Chem model domain configuration, including D01 (20 km) and D02 (4 km), and
 153 average base-model NO_x input emissions from EDGAR v5. D02 is centered over Thailand, and the urban signal associated
 154 with the Bangkok Metropolitan Region (BMR) is highlighted by the star.

155

156

157

158

159

160

161

162

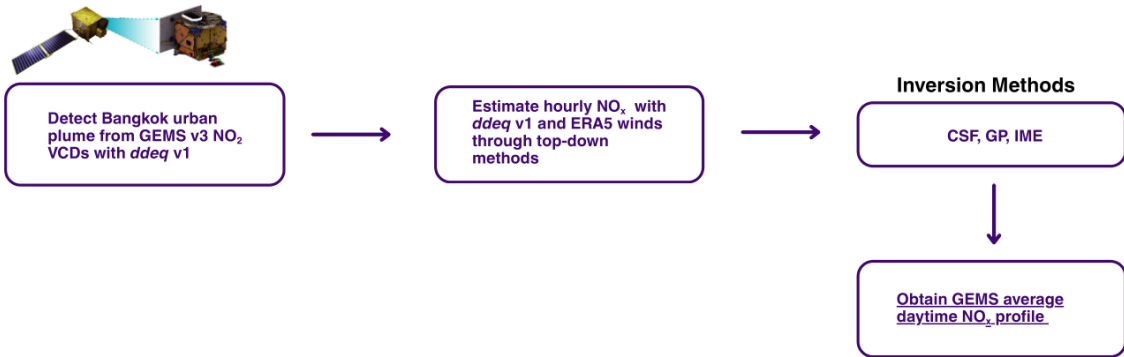
163

164

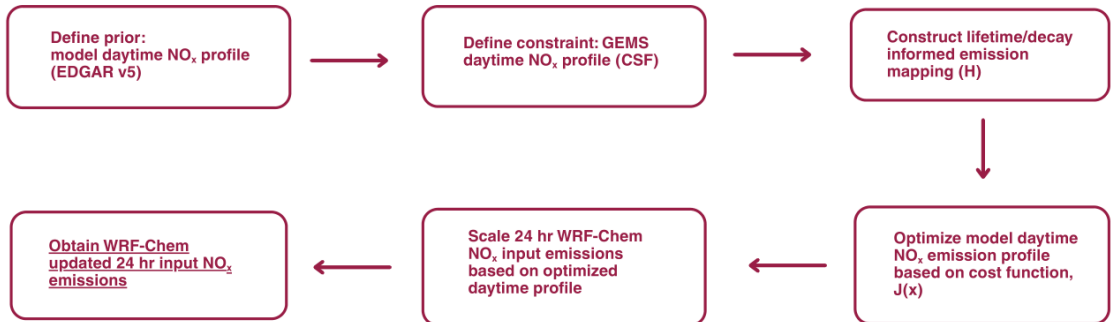
165

166

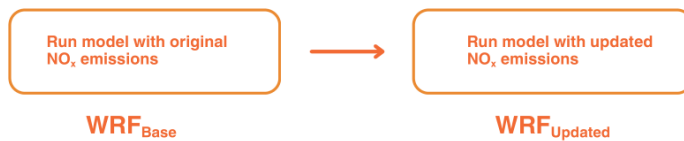
1 Estimate Daytime NO_x Emissions from GEMS



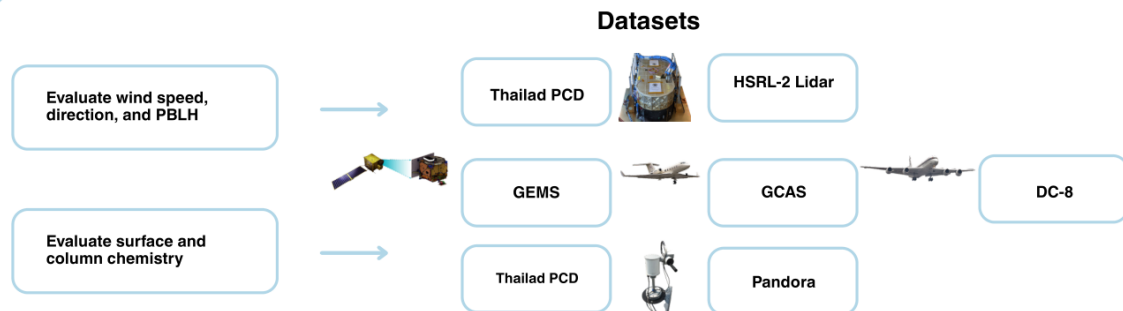
2 Correct WRF-Chem's NO_x Profile Based on GEMS



3 Test WRF-Chem NO_x Sensitivity



4 Evaluate WRF_{Base} and WRF_{Updated}



201 **Figure 2.** Schematic overview of the workflow used to derive satellite-constrained daytime NO_x emission profiles and assess
202 their impact in WRF-Chem over the BMR. (1) Urban NO₂ plumes are detected using GEMS tropospheric NO₂ columns, and
203 hourly NO_x emissions are estimated using top-down methods implemented in the *ddeg* v1 Python library. (2) a GEMS-derived
204 daytime NO_x profile is used to constrain the prior emission profile through an optimization framework, yielding updated input
205 24 h NO_x emissions for WRF-Chem. (3) Model simulations are performed using both the original and updated emissions. (4)
206 Model performance is evaluated against surface, column, airborne, and observations.

207 3 Satellite-derived NO_x emission estimates

208 3.1 Correcting for GEMS bias prior to inversion

209 Recent independent validation studies of the operational GEMS v3 product over Bangkok and South Korea report low biases
210 in NO₂ columns relative to ground-based sun-photometer and DOAS measurements (Bae et al., 2025; Jung et al., 2025). Bae
211 et al. (2025) shows that GEMS v3 increasingly underestimates NO₂ relative to Pandora under high-NO₂ conditions ($>1 \times 10^{16}$
212 molecules cm⁻²) as is the case for Bangkok pollution levels. In Jung et al. (2025), validation results over Bangkok indicate a
213 pronounced low bias in GEMS tropospheric NO₂ columns relative to Pandora, with regression slopes of ~ 0.35 for v2.0 and
214 ~ 0.28 for v3.0, indicating increasing underestimation at higher NO₂ levels. While moderate correlations ($r \approx 0.6\text{--}0.7$) suggest
215 that GEMS captures temporal variability, column magnitudes are substantially underestimated, particularly under polluted
216 conditions. The persistence of this behavior in the v3.0 product indicates that the low bias is not fully corrected by recent
217 algorithm updates and is consistent with retrieval sensitivity limitations in highly polluted urban environments (Jung et al.,
218 2025).

219 To address the low bias in GEMS prior to the NO_x satellite emission inversion, we first quantify the GEMS bias relative to
220 Pandora measurements over our period of interest (14 – 27 March 2024). We compare total column GEMS NO₂ to Pandora
221 Level 2 direct-sun total column retrieval, filtering for high quality measurements (quality flag = 10) and averaging to hourly
222 means. GEMS columns are sampled at the nearest grid cell to each Pandora site and temporally collocated. Results are shown
223 in Fig. S1. GEMS NO₂ columns are generally about a factor of two lower than Pandora measurements (mean bias $\approx -9.2 \times$
224 10^{15} molecules cm⁻²). This factor-of-two difference persists throughout March 2024 (Fig. S1).

225 To assess the sensitivity of the top-down NO_x inversion framework to this bias, we apply a simple correction factor to GEMS
226 prior to inversion. Specifically, GEMS NO₂ columns over the BMR are scaled by a factor of 1.67 derived from the Pandora
227 comparison. The inversion is then performed with and without the bias-corrected columns.

228

229 3.2 GEMS inversion framework

230 Previous studies have used satellite data (OMI, TROPOMI, SCIAMACHY, GOME (-2), OMPS) to estimate top-down NO_x
231 emissions over urban areas, but were limited to once-a-day, mid-afternoon measurements, leaving temporal variability in
232 emissions largely unaddressed (Beirle et al., 2011; Goldberg et al., 2017, 2019). Ground-based and aircraft measurements of
233 emissions can be challenging to constrain given boundary layer dynamics, such as changes in boundary layer height, stability,
234 and vertical mixing, which can strongly influence observed concentrations of trace gases (Goldberg et al., 2017, 2019).
235 Additionally, temporal allocation in bottom-up emission inventories remain a significant uncertainty, particularly at hourly
236 and daily timescales because default temporal profiles (diurnal, weekly, seasonal) often fail to capture real activity patterns,
237 meteorological influences, and sector-specific variability (Goldberg et al., 2017, 2019; Mues et al., 2014). GEMS observations,
238 however, offer a unique opportunity to provide hourly emissions rates over Bangkok, complementing existing inventories that
239 are usually provided at monthly scales. To estimate NO_x emissions over Bangkok in March 2024, we apply the methodology
240 of Kuhlmann et al. (2024), implemented through the openly available data-driven emission quantification (*ddeq v1*) Python
241 library (see step 1 Fig. 2). The standard *ddeq* library implements computationally inexpensive methods (e.g., Gaussian Plume
242 Inversion (GP), Cross-Sectional Flux (CSF) method, Integrated Mass Enhancement (IME) method) to estimate emissions from
243 Sentinel5P TROPOMI images (Graziosi and Manca, 2025; Meier et al., 2024). One study found limited temporal sampling
244 from polar-orbiting satellites (i.e., TROPOMI) can lead to systematic underestimation of NO_x emissions, particularly because
245 wintertime conditions with higher emissions are often poorly observed due to cloud cover (Meier et al., 2024). Geostationary
246 observations, including GEMS, address this limitation by providing hourly measurements that increase the likelihood of usable
247 data on partially cloudy days and enable direct resolution of daytime emission variability, which is not accessible from once-
248 daily LEO observations. For our application, we estimate emissions for daylight hours from GEMS tropospheric column NO₂
249 data over Bangkok during the ASIA-AQ campaign. A brief description of inversion methods and specifics is provided here. A
250 complete description of the inversion methods and algorithm can be found in Kuhlmann et al. (2024).

251
252 First, within the *ddeq* framework, the source location (Bangkok; 13.7563°N, 100.5018°E), GEMS v3 NO₂ column data, and
253 ERA5 wind fields are read. We chose to incorporate ERA5 wind fields as opposed to those provided by our high resolution
254 WRF-Chem simulation in this analysis given they presented significantly lower bias when compared to surface observations
255 (Fig. S2; Sect. 6.1). The ERA5 wind fields were downloaded and prepared by the *ddeq* library. Cloudy pixels (CF > 0.3) were
256 removed. Next, a plume detection algorithm is implemented to identify the Bangkok urban plume within the GEMS image.
257 The Bangkok plume subregion is estimated based on the source location and ERA5 wind field. Generally, a wind vector is
258 taken at the source location, and the plume is assumed to be located downwind, and a rectangular polygon can be drawn with
259 the along- and across- wind direction (Kuhlmann et al., 2024). An example of these plume detections and associated
260 rectangular polygons is shown in Fig. S3. To aid the algorithm's plume detection process, we identify two additional sources
261 north of Bangkok in the Saraburi province to avoid overlapping plumes from other NO_x sources. These correspond to the Khao

262 Wong (14.692856°N, 100.817204°E), and Thap Kwang (14.645313°N, 101.077650°E) regions, which we identified through
 263 NO₂ patterns visible in the GEMS data in Fig. S3. These areas are not representative of Bangkok urban emissions as they are
 264 a source of industrial activity related to limestone quarries and mining operations outside the inversion domain (Makkwao and
 265 Prueksasit, 2021). Next, a center curve is fitted to the data and natural coordinates are calculated for the detected plume
 266 associated to Bangkok to prep for the inversion algorithm. The coordinates are computed as the distance along and
 267 perpendicular to the wind vector and for curved plumes this distance is computed as the arc length. Lastly, the data is prepared
 268 for the satellite-derived emissions estimation by calculating and removing the background field and converting the NO₂
 269 columns to kg m⁻². We estimate satellite-derived NO_x emissions using three inversion techniques included in *ddeq*: CSF, GP,
 270 and IME methods. Below is a summary of the CSF method defined in Kuhlmann et al. (2024). GP and IME method descriptions
 271 are available in the Supplement (e.g., S1) and Kuhlmann et al. (2024). In the following subsections and in Section 4, we refer
 272 to the WRF-Chem input inventory based on EDGAR as the *prior emissions*, the CSF-based estimates from GEMS as the
 273 *satellite-derived emissions*, the CSF-based estimates from the model-simulated columns as the model-derived emissions, and
 274 the final emissions after applying the optimization framework, as the *posterior emissions*.

275

276 3.3 Cross-Sectional Flux (CSF) framework

277 The CSF approach applies mass conservation to quantify the NO_x flux transported downwind of Bangkok using (i) the wind
 278 speed perpendicular to the plume and (ii) the NO₂ enhancement integrated along the plume (line density). The NO_x flux, F (kg
 279 s⁻¹), is defined as:

$$280 \quad F = u \cdot q \quad (1)$$

281 where u (m s⁻¹) is the effective transport wind speed and q (kg m⁻¹) is the NO₂ line density. The emission rate, Q (kg s⁻¹), is
 282 then inferred by correcting for chemical decay along the plume using:

$$283 \quad Q = \frac{F(x)}{D(x,\tau)} \quad (2)$$

284 Here, $D(x, \tau)$ represents the along-plume decay for lifetime τ . Here, τ represents an effective plume lifetime that accounts for
 285 both chemical decay and plume dispersion (Kuhlmann et al., 2024).

286

287 3.3.1. Effective wind speed estimation

288 The *ddeq* algorithm computes an effective wind speed, i.e., the plume-transport wind, that supports an unbiased emission
 289 estimate. Ideally, this is a NO₂-enhancement-weighted average of the along-plume wind:

$$290 \quad u(x, y) = \frac{\int_0^{z_T} \rho_e(x, y, z) u(x, y, z) dz}{\int_0^{z_T} \rho_e(x, y, z) dz} \quad (3)$$

291 Here, $\rho_e(x, y, z)$ is the NO₂ enhancement, $u(x, y, z)$ is the along-plume wind speed and z_T is the plume-top height. Because
 292 ρ_e is not directly observed, *ddeq* follows the approximation of Fioletov et al. (2015), in which the effective wind speed is
 293 estimated using the mean of the lowest three ERA5 layers, representing the typical transport level for near-surface urban
 294 plumes.

295

296 3.3.2. NO₂ line density calculation

297 The line density $q(x)$, is the integral of the NO₂ enhancement across the plume cross-section:

$$298 \quad q(x) = \int_{y_1}^{y_2} (V(x, y) - V_{bg}(x, y)) dy \quad (4)$$

299 where $(V(x, y) - V_{bg}(x, y))$ represents the NO₂ enhancement above the background in kg m⁻². The integration bounds y_1 and
 300 y_2 are defined by the plume subregion (polygon) identified using the *ddeq* framework, which delineates the area of enhanced
 301 NO₂ associated with the source based on plume detection and wind direction (Kuhlmann et al., 2024). As such, the effective
 302 integration length across the plume is determined by the spatial extend of this polygon and the fitted Gaussian representation.
 303 To further compute this and account for missing satellite pixels, *ddeq* fits a Gaussian function to all GEMS pixels within a
 304 plume polygon:

$$305 \quad g(y) = \frac{q}{2\sqrt{\pi}\sigma} \exp \exp \left(-\frac{(y - \mu)^2}{2\sigma^2} \right) + my + b \quad (5)$$

306 Here, μ and $\sigma(x)$ are the plume center and width in meters, and $my + b$ approximates a linear background. The plume width
 307 is further defined as:

$$308 \quad \sigma(x) = \sqrt{\frac{2Kx^\kappa}{u}} \quad (6)$$

309 Where K is the eddy diffusivity coefficient (m² s⁻¹), κ accounts for nonlinear plume spreading under varying meteorology, and
 310 u is the effective transport wind speed defined above. The plume width, $\sigma(x)$ is derived from the Gaussian fit, and the
 311 parameters, K and κ are then determined by fitting, $\sigma(x)$ within the CSF framework. After fitting the Gaussian function, line
 312 densities are converted to fluxes using wind speeds at each corresponding downwind cross-section. Fluxes can be estimated
 313 for several cross-sections or polygons located downwind of the urban source (see Fig. S3,S4) (Kuhlmann et al., 2024). Using
 314 multiple points along the plume ensures different portions of the plume are sampled robustly.

315

316 3.3.3. Emission rate and lifetime estimation

317 Because NO₂ decays as the plume travels, the flux decreases with distance. To estimate the true emission rate, Q , at the source,
 318 *ddeq* fits a lifetime τ by matching modeled and observed flux decay:

$$319 \quad F_a(x, \tau, \mu_a, \sigma_a) = Q \int_{-\infty}^{\infty} D(x', \tau) g(x - x', \mu_a, \sigma_a) dx' \quad (7)$$

320 Where μ_a and σ_a describe the city-scale plume location and extent, $D(x', \tau)$ describes the exponential decay along the plume,
321 and g is the Gaussian parameter described above. Fitting Eq. (7) to the derived fluxes yields both the emission rate Q and
322 plume lifetime τ (Kuhlmann et al., 2024).
323

324 3.3.4. Conversion from NO₂ to NO_x emissions

325 GEMS provides NO₂ column densities; therefore, a NO₂-to-NO_x conversion factor is needed to obtain NO_x emissions.
326 Following the *ddeg* implementation, we use:

$$327 Q_{NO_x} = f_q \cdot Q_{NO_2} \quad (8)$$

328 to obtain NO_x estimates, where $f_q = 1.32$, as implemented in the *ddeg* algorithm; a localized factor was not derived from WRF-
329 Chem due to known NO₂ biases in the prior simulation that would propagate into the conversion.
330

331 3.3.5 Structural uncertainties in the CSF framework

332 While the CSF framework provides a computationally efficient approach for deriving satellite-derived emissions, we
333 acknowledge the method contains some structural uncertainties. First, the integration bounds used to compute the line densities
334 (Eq. 4) are defined by the plume polygon identified from the satellite observations and wind field, such that the inferred top-
335 down emissions depend on how the plume extent is delineated. As a result, inferred satellite-derived emissions can be sensitive
336 to the selected plume extend, particularly under conditions of weak enhancements or overlapping sources. Second, the satellite-
337 derived emission estimate scales directly with the effective wind speed (Eq. 1), such that errors in wind magnitude or direction
338 propagate into the derived fluxes and satellite-derived emissions (see Fig. S5). Although ERA5 winds averaged over the lowest
339 model layers are used to approximate plume transport, they may not fully represent local meteorological variability. Third, the
340 inferred satellite-derived emission rate depends on the assumptions within the fitting framework, including the Gaussian
341 representation of plume structure (Eq. 5), the parametrization of plume spreading (Eq. 6), and the effective lifetime τ (Eq. 7),
342 which represent a simplified treatment of chemical decay and dispersion. Together, these factors represent inherent
343 uncertainties in the CSF approach that should be considered when interpreting the satellite-derived emissions.
344

345 3.4 Results for satellite-derived NO_x emission estimates

346 GEMS NO_x emissions for Bangkok were estimated for daytime hours (00:45:00 – 06:45:00 UTC) during the ASIA-AQ
347 deployment, 14 – 27 March 2024. The bias-corrected satellite inversion results are denoted with the subscript “BC”. Days
348 with significant cloud contamination were removed from the analyses on a case-by-case basis, leaving satellite-derived
349 emissions estimates for 14,15,17,18,22,24,25 March 2024. Satellite-derived emissions were computed for both weekends and

350 weekdays, however, due to fewer weekends in the study period, weekday estimates are estimated to be more robust. We
351 aggregate satellite-derived emissions hourly across weekdays to produce a summary daytime profile as illustrated in Fig. 3a
352 and Fig. 3b. Satellite-derived emissions generally range between 0.5 – 4 kg s⁻¹ dependent on the inversion method. Bias-
353 corrected results (Fig. 3b) illustrate a larger NO_x range, between 0.4 – 5 kg s⁻¹. Differences between CSF, GP, and IME satellite-
354 derived emission estimates are expected, as each method relies on distinct assumptions regarding transport, plume geometry,
355 and chemical loss. Similar spreads between methods have been reported in previous satellite-based emission studies
356 (Hakkarainen et al., 2023, 2024; Santaren et al., 2025), particularly in urban environments, and can be interpreted as a measure
357 of structural uncertainty rather than inconsistency between methodologies. Nevertheless, in this application, the CSF method
358 illustrates a distinct daytime pattern with satellite-derived emissions peaking between 08:00:00 – 09:00:00 LT (bias-corrected)
359 coinciding with morning rush hour traffic, decreasing by approximately 65% by 14:00:00 LT. The GP and IME results illustrate
360 a relatively stable daytime pattern and overall lower (< 50%) morning satellite-derived emission compared to the CSF method.
361 These results reflect both methodological differences and uncertainties in the underlying NO₂ observations. While the satellite-
362 derived emissions might provide strong constraints on daytime variability, uncertainties in the GEMS NO₂ retrieval,
363 particularly under high NO₂ conditions may influence the magnitude and timing of the inferred emissions as depicted in Fig.
364 3a,3b. The bias-corrected emissions are approximately 70% higher on average, indicating a substantial sensitivity of the
365 inversion to the assumed retrieval bias.

366

367 **3.5 Selection of the inversion method**

368 To identify the optimal inversion method to be used for model correction, we test which method can successfully recover
369 WRF-Chem’s prior daytime NO_x emission profile. To do so, we apply the *ddeq* inversion algorithms to WRF_{Base}, to produce
370 “top-down” estimates from the model, which we will refer to as model-derived emissions. To replicate the satellite output, we
371 re-gridded the model output from its native resolution to the satellite swath grid using the Universal Regridder for Geospatial
372 Data (xESMF) Python package (Jiawei Zhuang et al., 2025). A nearest-neighbor interpolation scheme was used to preserve
373 spatial gradients and align the model resolution to that of the satellite observations. This spatial re-gridding was performed on
374 an hourly basis, corresponding to the nearest observation time (00:45:00 – 06:45:00 UTC). Following re-gridding, model NO₂
375 mixing ratios were vertically interpolated to the satellite pressure levels using a one-dimensional linear interpolation to ensure
376 consistency between the model and observed data for averaging kernel application. After interpolating model output to
377 GEMS’s spatial and pressure grid, we computed the model’s tropospheric column NO₂ (molecules cm⁻²). This is done by
378 converting the model’s standard output of NO₂ volume mixing ratio (ppmV) to a number density with the ideal gas law:

$$379 \quad NO_{2\text{Number Density}} = \frac{P \cdot \chi_{NO_2} \cdot N_A}{R \cdot T} \quad (9)$$

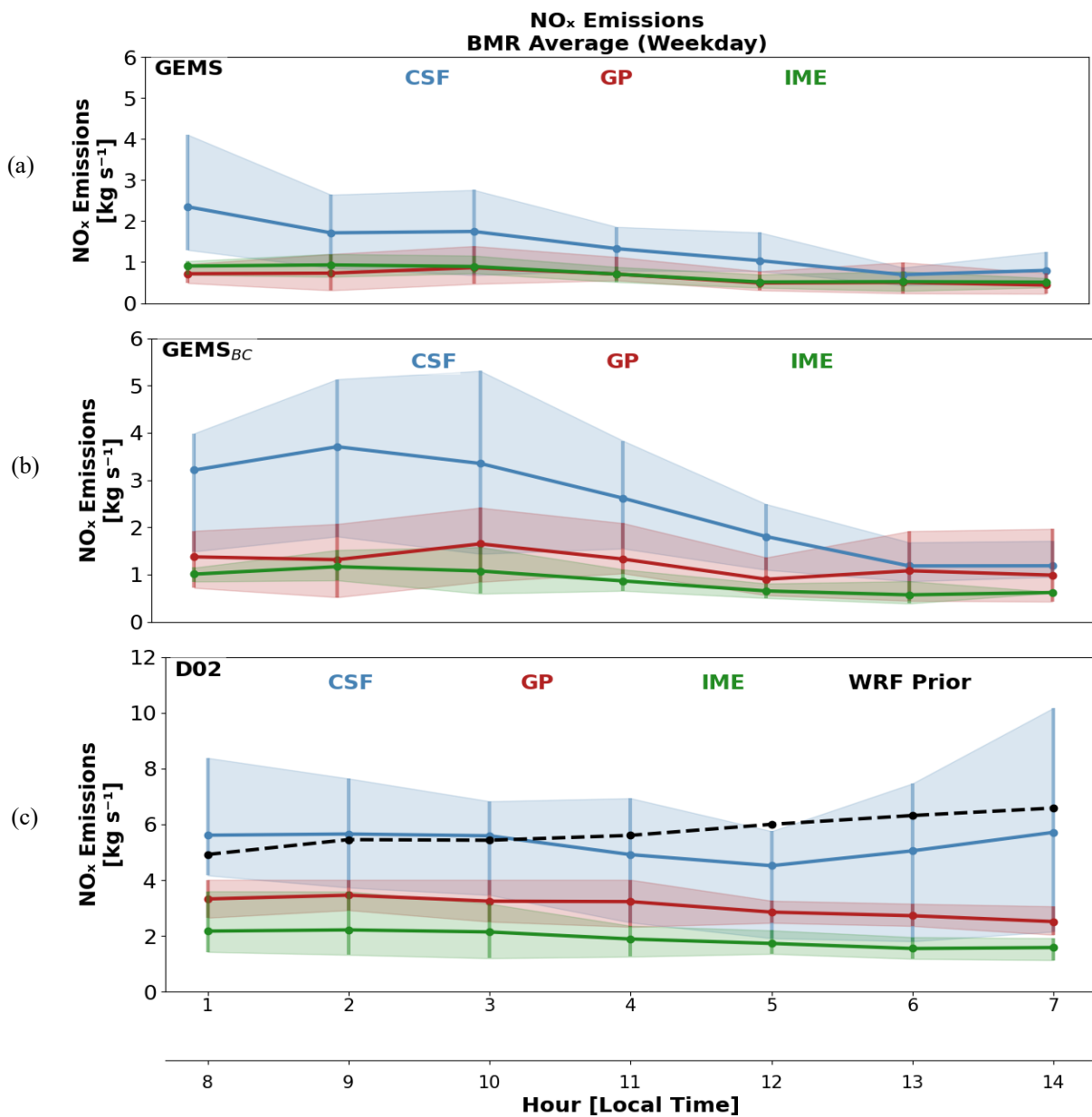
380 Where χ_{NO_2} is the NO_2 mixing ratio in ppmV, P is pressure in Pa, T is temperature in K, R is the gas constant (8.314 J/mol/K),
381 and N_A is Avogadro's number ($6.022 \times 10^{23} \text{ mol}^{-1}$). The number density is then multiplied by the thickness of each vertical
382 model layer Δz to obtain the NO_2 amount per unit area. Summing across all layers yields the total column NO_2 :

$$383 \quad NO_{2WRF-GEMS} = \frac{1}{10^4} \times \sum_k (A_k \cdot NO_{2Number\ Density,k} \cdot \Delta z_k) \quad (10)$$

384 Where A_k is the averaging kernel value at layer k , Δz_k is the thickness of the model layer k , in meters, and $\frac{1}{10^4}$ converts the
385 units to molecules cm^{-2} . As WRF-Chem has no stratosphere, we regard this as the tropospheric column NO_2 . The satellite
386 averaging kernel weights each model layer based on how sensitive GEMS is to that part of the atmosphere. This allows for a
387 direct comparison with GEMS retrievals.

388

389 We compute model-derived NO_x emissions from re-gridded WRF_{Base} (which we denote as WRF-GEMS) with *ddeq* and the
390 resulting average daytime profile for Bangkok is illustrated in Fig. 3b, 3c. The shape and magnitude of model-derived NO_x
391 emissions differ substantially from the satellite-derived emission data. Model-derived emissions are initially > 50% larger than
392 GEMS-derived emissions. Additionally, there are minimal changes in the daytime pattern present in any of the inversion
393 methods. In fact, WRF-GEMS D02 sees an increase in emission between 08:00:00-10:00:00 LT, a pattern that disagrees with
394 the observed satellite-derived emissions. The results here further illustrate the need for an hourly correction to the model's
395 emission profile, rather than applying a single scaling factor across all hours. The WRF_{Base} prior emission profile is shown by
396 the black dashed line. For this comparison, we smoothed the prior emission profile using a 3 h backward-looking average to
397 account for the accumulation and chemical evolution represented implicitly in the inversion results. Overlaying the prior
398 emissions shows that the model-derived CSF method most accurately recovers them, likely due to its use of downwind fluxes
399 and multiple cross-sections across the plume, which provide additional constraints on plume evolution and reduce sensitivity
400 to local errors in wind fields, plume definition, and missing data compared to the IME and GP methods. As a result, we select
401 the CSF inversion method moving forward to correct and scale WRF-Chem's daytime NO_x emission profile.



402

403

404 **Figure 3.** Comparison of daytime NO_x emission estimates derived from (a) GEMS, (b) GEMS with bias correction applied

405 (GEMS_{BC}), and (c) WRF-GEMS D02 using the Cross-Sectional Flux (blue), Gaussian Plume inversion (red), and Integrated

406 Mass Enhancement (green) methods. Emissions (kg s⁻¹) represent averages across daytime hours and weekdays during the

407 ASIA-AQ deployment period (14 – 27 March 2024). Model-derived emissions in (b) and (c) were obtained by re-gridding

408 WRF_{Base} output to the GEMS spatial resolution and applying the same inversion methods. The WRF_{Base} prior emission profile

409 is shown as a black dashed line and represents a backward-looking three-hour average to account for emission accumulation
410 embedded in the inversion estimates.

411

412 **4 Model emission adjustment framework**

413 To better represent NO_x emissions over Bangkok, we developed an optimization framework to re-scale and shape WRF-
414 Chem’s prior daytime emissions across the BMR (see step 2 Fig. 2). The prior emissions come from monthly EDGAR v5
415 values. The optimization uses a cost function $J(x)$ to adjust daytime prior emissions based on GEMS NO_x retrievals,
416 incorporating the lifetime and uncertainties from both the model and observations.

417 **4.1 Optimization of daytime anthropogenic NO_x emissions**

418 **4.1.1. Observational constraint**

419 The GEMS average daytime NO_x profile (blue lines in Fig. 3a,3b) from the CSF method provides the observational constraint.
420 Two versions of the optimization are performed: one using the constraint derived from the bias-corrected retrievals, and one
421 without it. To improve consistency between the observed and modeled columns, we applied a correction factor to the constraint
422 to account for the portion of the NO₂ column that GEMS does not capture because of reduced sensitivity near the surface.
423 Although the air mass factor (AMF) calculation includes vertical weighting, the retrieved GEMS column can still
424 underestimate tropospheric NO₂ in conditions where a substantial fraction resides in the lowest few hundred meters and is
425 weakly sensed by the instrument. To address this sensitivity, satellite-derived NO_x emission estimates were scaled using the
426 ratio of model-derived emissions obtained from the full column (i.e., Eq. (10) excluding the A_k) and from the same column
427 after application of the GEMS averaging kernel:

$$428 \quad y = e_{GEMS} \times \left(\frac{e_{WRF}^{TC}}{e_{WRF}^{AK}} \right) \quad (11)$$

429 Where e_{GEMS} , e_{WRF}^{TC} , and e_{WRF}^{AK} denote the satellite-derived -derived daytime NO_x emission profiles derived from GEMS,
430 model-derived emissions from WRF-Chem (D02) total columns, and model-derived emissions from the same columns after
431 applying the GEMS averaging kernel, respectively. Hourly correction factors ranged between 1.05 – 1.33, where larger
432 corrections (e.g., 1.33) were present in the morning hours, 01:00:00 – 02:00:00 UTC. This vertically adjusted satellite-derived
433 emission vector was used as the observational constraint, y , in the optimization.

434

435 **4.1.2. Prior assumptions, lifetimes, and temporal weighting**

436 The prior for the optimization, x_b , refers to the bottom-up daytime NO_x emission profile shown in the black dashed line in Fig.
437 3b. For the optimization, it is necessary to map the prior emissions to the satellite-derived emissions through the observational

438 operator H . Satellite emissions of NO_x represent not only emissions from the current hour, but also contributions from
 439 preceding hours. To address this, we introduce an operator H that links the prior daytime hourly emissions to the satellite-
 440 derived NO_x amounts. Each row of H defines how emissions from a set of prior model hours contribute to an observation at
 441 time, t_i .

442

443 For each GEMS observation hour t_i , we assume that the column enhancement is influenced by emissions from a backward-
 444 looking window of three model hours:

$$445 \quad t_i - 2, t_i - 1, t_i$$

446 The window choice was determined by comparing inversion results to model priors using averaging windows from 1 – 6 hours.
 447 The three-hour window provided the best agreement with the model-derived CSF emissions as shown in Fig 3b, 3c. Within
 448 this window, the contribution from each prior hour depends on the atmospheric lifetime of NO_2 for that hour. We use hourly
 449 lifetimes, τ , derived from the GEMS-based CSF inversion in Eq. (7), where τ is fitted from observed along-plume decay using
 450 ERA5 winds, and is therefore independent of WRF-Chem meteorology. This ensures the satellite-derived emission estimates
 451 are completely independent of the WRF-Chem simulations. For reference, WRF-Chem-derived decay times are generally
 452 longer than those inferred from GEMS, reflecting differences in modeled vs. observed loss and dilution processes. Hours with
 453 no satellite information, are assigned a default lifetime of 3 hours. We then apply a simple exponential decay law:

$$454 \quad w(\Delta t) = \exp\left(-\frac{\Delta t}{\tau}\right) \quad (12)$$

455 where:

$$456 \quad \Delta t \in \{0,1,2\}$$

457 is the time lag between when NO_x was emitted and when its NO_2 enhancement is observed. These raw weights are normalized
 458 within each row of H to ensure mass conservation:

$$459 \quad H_{i,j} = \frac{w(\Delta t_j)}{\sum_{j'} w(\Delta t_{j'})} \quad (13)$$

460 Thus, $H_{i,j}$, represents the fraction of the observed column at hour i , that is attributable to emissions from model hour j . This
 461 framework of H ensures that shorter lifetimes contribute to a stronger emphasis on the most recent emissions, appropriately
 462 reflecting rapid chemical loss, and longer lifetimes spread the influence of emissions over multiple hours, consistent with
 463 slower decay. By embedding this chemical persistence into the operator, H , we obtain a physically representative mapping
 464 between model emissions and the satellite observations that are used to constrain them.

465

466 4.1.3. Solution for posterior daytime emissions

467 A model corrected daytime NO_x emission profile (posterior), \hat{x} was obtained by minimizing the following cost function:

$$468 \quad J(x) = \frac{1}{2}(y - Hx)^T R^{-1}(y - Hx) + \frac{1}{2}(x - x_b)^T B^{-1}(x - x_b) \quad (14)$$

469 Where y is the satellite-derived, column-corrected NO_x emission vector, x is the unknown corrected model daytime emission
470 profile, x_b is the model prior profile, $R = \sigma_I^2 I$, $B = \sigma_B^2 I$ are the observation and background error covariance matrices, and
471 H is the observational operator matrix described above. In this study, we use $R = 1$ and $B = 10$. These values were based on
472 sensitivity tests in which we vary R and B over several orders of magnitude. The chosen values represent a compromise that
473 allowed the posterior emission profile to closely follow the satellite constraints while preventing excessive deviations from the
474 prior emission profile. To account for temporal correlation in prior emission errors, the elements of B are defined as:

$$475 \quad B_{i,j} = \sigma_B^2 \exp\left(-\frac{|t_i - t_j|}{L}\right) \quad (15)$$

476 Where $|t_i - t_j|$ is the temporal separation between emission hours i and j , and L is the temporal correlation length, set to $L =$
477 2 hr in this study. This setup ensures that prior errors vary smoothly in time rather than independently hour-to-hour. Finally,
478 the cost function was minimized using a Sequential Least Squares Quadratic Programming (SLSQP) algorithm
479 (minimize(method='SLSQP') — SciPy v1.16.2 Manual, 2025; Nocedal and Wright, 2006). The result is a corrected model
480 hourly emission vector, \hat{x} , that balances the satellite-derived emissions with the model's prior estimate while accounting for
481 chemistry and transport behavior (Fig. 4).

482
483 Figure 4a and 4c illustrate the raw hourly daytime NO_x for both the prior model (dashed purple) and the optimized version
484 (solid purple), based on constraints applied without and with the GEMS bias correction, respectively. In both bases, the
485 posterior profile departs notably from the prior in both magnitude and shape. In the case without the bias-corrected constraint
486 (Fig. 4a), a morning peak is visible at 07:00:00 LT, followed by a steady decline until 13:00:00 LT. This pattern is consistent
487 with temporal patterns in weekday traffic intensity in Bangkok found in Ly et al. (2015), which found the morning traffic to
488 peak at 07:30:00 LT ending at 09:30:00 LT, and the evening peak from 17:00:00 to 20:00:00 LT (outside of GEMS observing
489 window). Activity begins to increase at 13:00:00 LT which corresponds to the NO_x increase we begin to see in the posterior
490 result after 06:00:00 UTC. The case with the bias-corrected constraint (Fig. 4c) places peak morning emission closer to the
491 model prior at 07:00:00 – 08:00:00 LT, with NO_x declining slightly later, at 09:00:00 LT. NO_x emission begins to increase
492 after 13:00:00 LT similar to what is depicted in Fig. 4a. When the prior and posterior hourly emissions are passed through H ,
493 we obtain a temporally smoothed emission profile consistent with what GEMS would observe (Fig. 4b,4d). Figures 4b and 4d
494 show the posterior profile closely reproduces the GEMS-derived daytime pattern, indicating the optimization effectively aligns
495 model emissions with satellite-derived emissions while preserving components of the prior model behavior.

496 **4.2 Adjustment of WRF-Chem diurnal emission profiles**

497 Using satellite-derived NO_x emissions and the posterior results above, we correct the WRF-Chem 24 h input emissions over
498 the BMR. Since GEMS provides estimates over 01:00:00-07:00:00 UTC, we only have posterior model emissions over this
499 window. To apply these updates to the full gridded 24 h WRF-Chem anthropogenic emission input (00:00:00-23:00:00 UTC),
500 while preserving the model's spatial distribution, we compute hourly scaling factors which we use to adjust the gridded prior

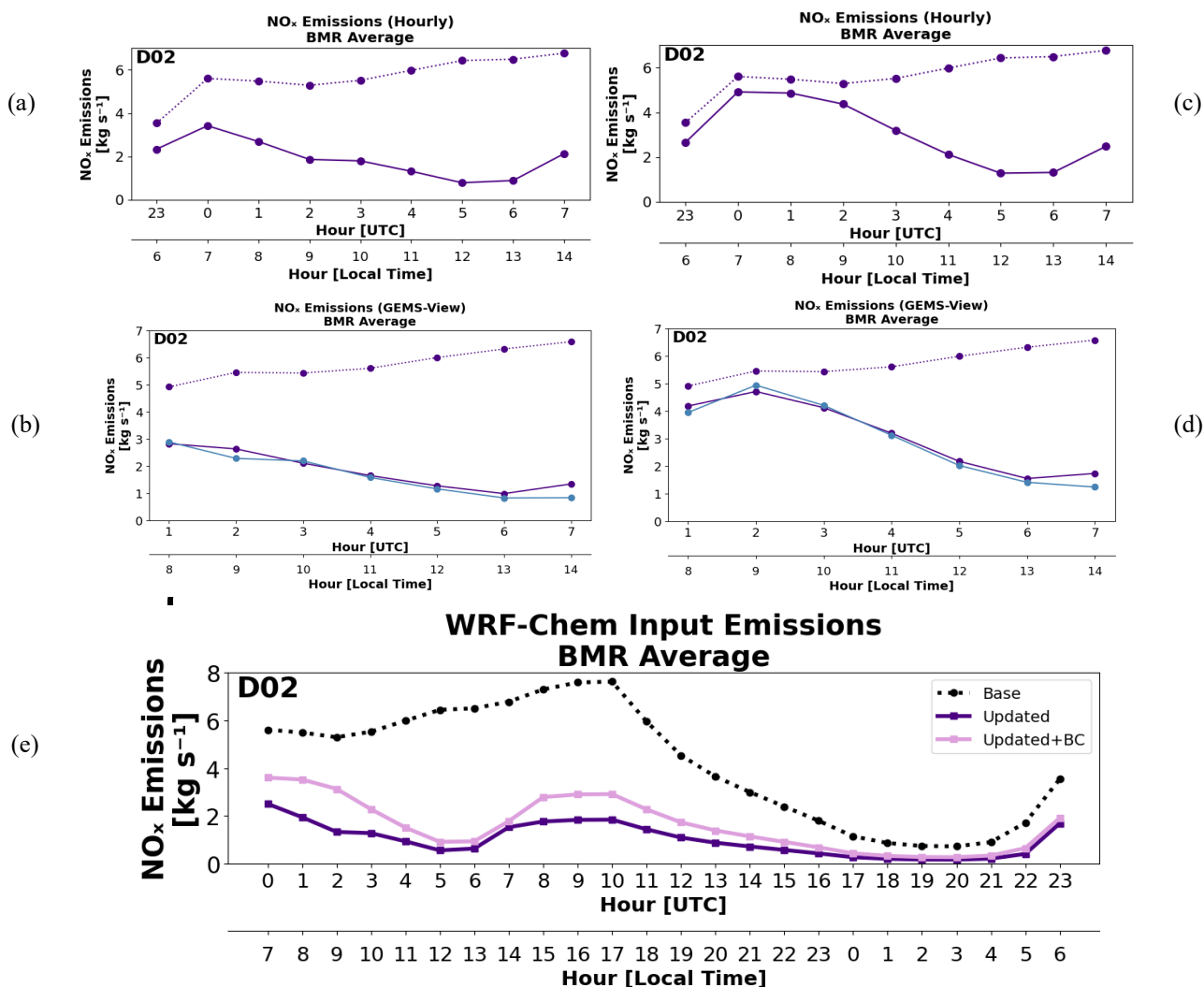
501 NO_x emissions. Because GEMS provides constraints only during the daytime overpass window, the derived scaling below
502 primarily reflects daytime emission adjustments. We therefore apply the mean scaling factor uniformly during the nighttime
503 hours to preserve the prior temporal structure and avoid introducing artificial discontinuities between the constrained and
504 unconstrained hours, particularly given the large daytime emission reductions. This approach is consistent with previous
505 satellite-constrained emission studies (e.g., Goldberg et al., 2019) which constrain emission magnitude based on a single
506 daytime value derived from OMI. Where available, locally derived temporal profiles should be used to better represent regional
507 emission patterns; in this study, our prior profile reflects the best available regional representation for Asia at the time of study.
508

509 To compute the factors, hourly WRF-Chem NO and NO₂ prior emission fields were summed across the vertical levels and
510 masked to the Bangkok region bounded by N-S:13.5°-15.0°, W-E:100.2°-100.9°, using the WRF-Chem grid. In WRF-Chem,
511 NO_x emissions are stored as NO₂-equivalent mass ('NO_x-as-NO₂'), so all conversions use the molecular weight of NO₂. The
512 total emissions were converted to mol hr⁻¹ using a molecular weight of 46.01 g mol⁻¹ and an area of 16 km² per grid cell
513 (following the resolution of D02). Each posterior emission, \hat{x}_h was converted from kg s⁻¹ to mol hr⁻¹ and divided by the
514 corresponding original WRF-Chem total to compute a scale factor, f for each hour h :

$$515 \quad f = \frac{\hat{x}_h \times \frac{1000}{46.01} \times 3600}{E_H^{WRF}} \quad (16)$$

516 Where E_H^{WRF} is the original domain-integrated prior NO_x emissions for hour h . Since the optimization covered hours with
517 GEMS measurements, the scaling factors for the remaining model hours were computed using the ratio of average daytime
518 posterior emissions where averages are taken over the constrained hours. Finally, we apply the scaling factors spatially over
519 the BMR. The scaling factor was applied to the hourly WRF-Chem anthropogenic emissions prior files and only to NO and
520 NO₂ grid cells within the BMR mask. This preserves the original spatial distribution but adjusts the total prior emissions to
521 match the posterior values. The updated emission files were then used to initialize an updated model simulation, ran for the
522 ASIA-AQ deployment period, which we will refer to as WRF_{Updated} (see step 3 Fig. 2).
523

524 Figure 4e compares the average diurnal prior profile over BMR with the updated profile derived from the optimization and
525 scaling procedure. The optimized diurnal profile based on the bias-corrected GEMS constraint is illustrated by the light pink
526 line. The updated profiles show a notable increase in NO_x between 07:00:00-10:00:00 UTC (14:00:00 to 17:00:00 LT), which
527 may reflect the beginning of a rush-hour signal over the city. Nighttime emissions retain the overall shape of the prior profile
528 but are scaled downward based on the daytime average. Figure S6 maps the spatial distribution of these updates across BMR,
529 showing the largest differences in the late afternoon and early evening, with localized reductions of up to 400 mol km⁻² hr⁻¹ in
530 the updated input emissions.
531
532
533



535

536

537 **Figure 4.** Results of the emissions optimization, shown as averages over the BMR. (a) Posterior optimized (solid) and prior
 538 (dashed) daytime NO_x emissions in model space, where the prior represents the three-hour backward average of EDGAR v5
 539 emissions used as input to the optimization. (b) Same emissions as in (a) but transformed into observational space using the
 540 observational operator. The GEMS profile is shown in blue. (c) and (d) are representative of optimization results using the
 541 GEMS bias-corrected CSF results as the constraint. (e) Full diurnal cycle of updated (solid purple), updated+BC (solid pink),
 542 and prior (dashed) NO_x emissions. Note that, unlike (a), the prior in (e) does not include the 23 UTC hour from the previous
 543 day in the backward averaging.

544

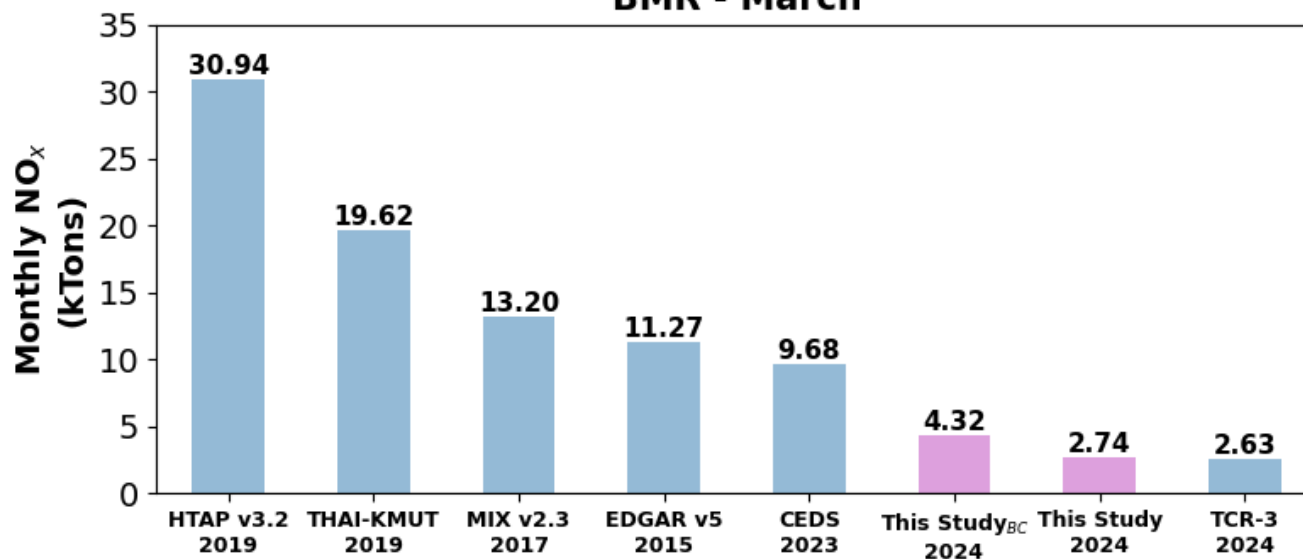
545 4.3 Comparison with bottom-up emission inventories

546 To place the updated NO_x emissions in context of existing emission inventories, we compared total monthly emissions over
547 the BMR against several widely used bottom-up inventories, our top-down emissions (including bias-corrected results – This
548 Study_{BC}), and emissions from a chemical reanalysis product (Fig. 5). These include HTAP v3.2 (base 2019), a local Thailand
549 Inventory (THAI-KMUTT) (base 2019), MIX v2.3 (base 2017), EDGAR v5 (base 2015), CEDS (base 2024), our study (2024),
550 and the Tropospheric Chemistry Reanalysis (TCR-3) top-down emissions TCR-3 (2024) (Miyazaki et al., 2020). Across
551 inventories, monthly totals for March can vary nearly by an order of magnitude, highlighting large uncertainty in regional NO_x
552 sources and emissions processing methodology. For example, although both HTAP v3.2 and MIX v2.3 rely on the REAS
553 framework (Kurokawa and Ohara, 2020) for Asian anthropogenic emissions, they are derived from different REAS versions,
554 temporal coverage, and processing assumptions, which can lead to substantial differences in absolute emission magnitudes
555 over Bangkok. HTAP v3.2 is based on REAS v3.2.1, which provides monthly emissions for 2000–2015 at a spatial resolution
556 of 0.25°. In the HTAP product, these emissions are re-gridded to 0.1° by assuming a uniform spatial distribution within each
557 grid cell (Guizzardi et al., 2025). In contrast, the MIX inventory is based on REAS v2, which covers 2000–2008 and reflects
558 earlier emission estimates and activity data (Li et al., 2024). REAS v2 was subsequently extended to 2010 following the scaling
559 approach described by Kurokawa & Ohara (2020).

560
561 Overall, HTAP v3.2 depicts the highest NO_x totals at 31kTons month⁻¹. THAI-KMUTT follows with emissions at ~20 kTons
562 month⁻¹, reflecting its incorporation of detailed regional activity from local emissions data. The coarser-resolution MIX v2.3,
563 and EDGAR v5, and CEDS inventories reflect lower totals, at ~13,11,10 kTons month⁻¹ respectively, consistent with the use
564 of different emission estimation methodology and older base years for MIX and EDGAR which correspond to lower macro-
565 economic (e.g., GDP) indicators in Thailand compared to 2019. Lastly, GEMS top-down NO_x estimates (including bias-
566 corrected results) and TCR-3 estimates based on the chemical reanalysis using TROPOMI NO₂ indicate substantially lower
567 emissions (2-4 kTons month⁻¹). These reduced magnitudes may result from both recent emission declines and structural
568 differences in how emissions are computed (i.e., top-down perspective).

569
570 It is important to note uncertainties are present and differ amongst emission methods. For example, bottom-up inventories
571 depend on activity data, emission factors, spatial approximations, and assumptions that may not capture rapid socio-economic
572 changes or region-specific behavior. Top-down estimates incorporate uncertainties from their respective satellite retrievals,
573 reanalysis data (e.g., ERA5), averaging kernels, chemical lifetime assumptions, and forecast-model transport and chemistry
574 (e.g., TCR-3). Together, these differences highlight the value of combining observational constraints with updated bottom-up
575 information to define NO_x emission estimates.

NO_x Inventory Comparison BMR - March



576

577

578

579

580

581

582

583

584

Figure 5. Comparison of March NO_x emissions over the BMR derived from bottom-up, top-down, and assimilated approaches. Bottom-up inventories (HTAP v3.2 (Guizzardi et al., 2025), THAI-KMUT, MIX v2.3 (Li et al., 2024), EDGAR v5 (Crippa et al., 2020), and CEDS (Hoesly et al., 2018)) exhibit substantial variability. In contrast, top-down estimates from GEMS and TROPOMI (TCR-3) for 2024 indicate considerably lower emissions (2.6–4.3 kt month⁻¹), highlighting uncertainties in bottom-up inventory methodologies, satellite sensitivity, and potential changes in anthropogenic NO_x activity.

585

5 Evaluation against satellite observations

586

587

588

589

590

591

592

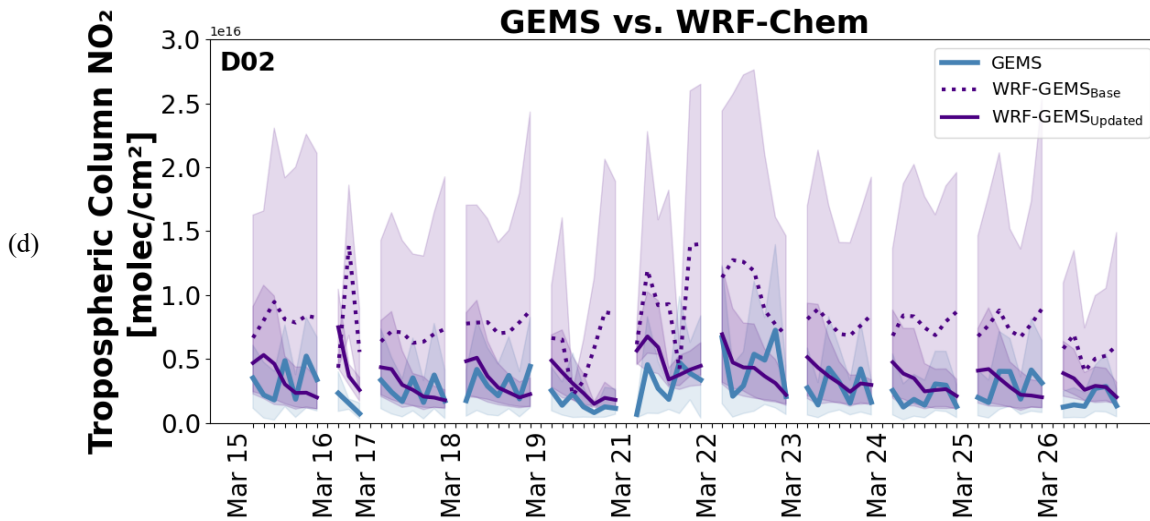
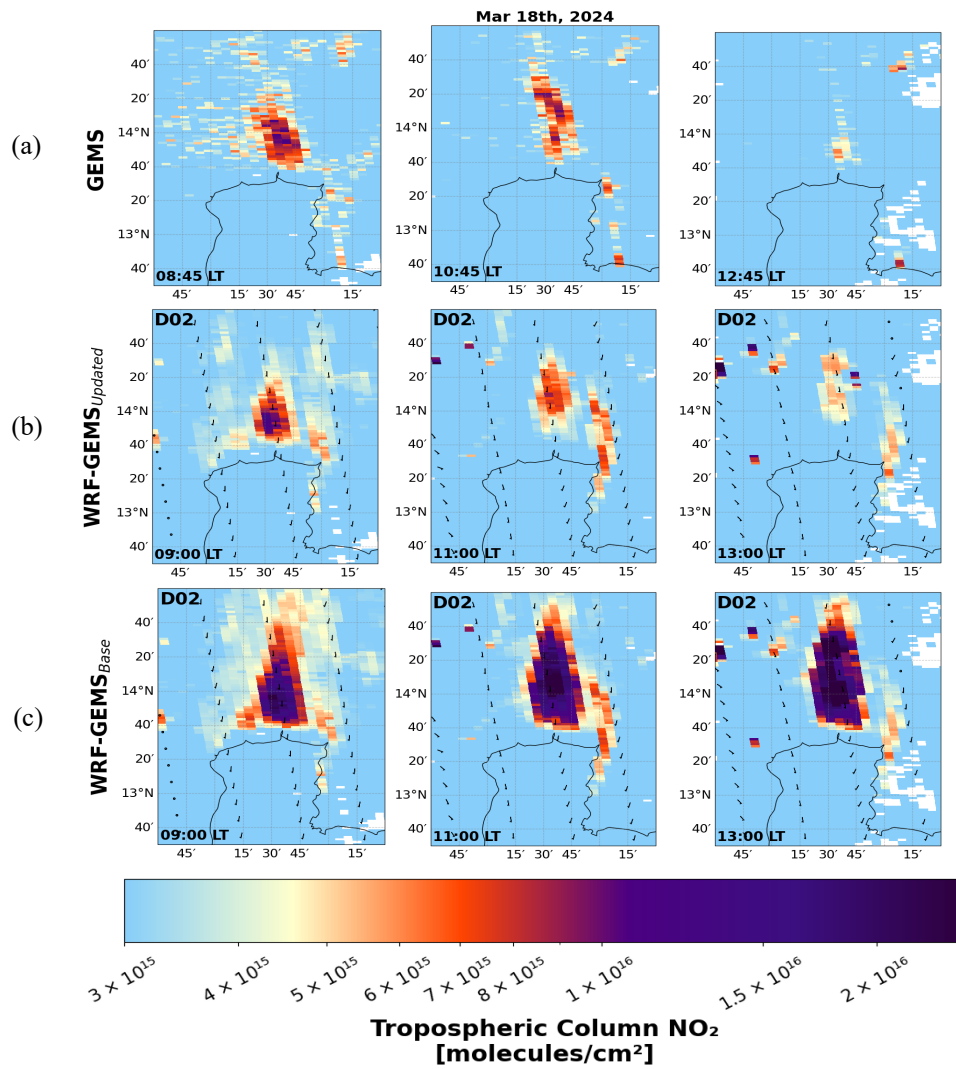
593

To evaluate the performance of WRF-Chem (Base + Updated) NO₂ simulations during the ASIA-AQ period (14 – 27 March 2024) in Bangkok, we first compared model output with satellite tropospheric column NO₂ retrievals from GEMS v3 data. For GEMS observations, pixels were filtered based on cloud fraction (CF < 0.3). The GEMS averaging kernel and air mass factor data were used to isolate tropospheric contributions and account for satellite instrument sensitivity. To enable a direct comparison with our model output, we re-gridded model output from its native resolution to the satellite swath grid as explained in Sect. 3.3. As before, refer to the re-gridded model simulations with the GEMS averaging kernel applied as WRF-GEMS. To evaluate regional NO₂ variability, we aggregated satellite and model-derived tropospheric column NO₂ values over the BMR, by defining a N-S (13.5-14°N), W-E (100.3-100.9°E) bounding box for the area. For pixels within this boxed region,

594 we calculate the mean NO₂ concentration, minimum NO₂, maximum NO₂, standard deviation, and the 10th and 90th percentiles
595 to characterize regional variability. This analysis was repeated on an hourly basis for each co-located WRF-Chem and GEMS
596 dataset, providing a regionally aggregated view of column NO₂ for intercomparison.

597
598 The results shown here are based on satellite comparisons using the non-bias corrected model results and are intended to
599 illustrate that the optimization brings the model closer to GEMS observations. The maps shown in Fig. 6 illustrate a spatial
600 comparison of (a) GEMS, (b) updated model results, WRF-GEMS_{Updated} D02, and (c) base model, WRF-GEMS_{Base} D02
601 tropospheric columns NO₂ over the BMR for several snapshots on 18 March 2024. Results for D01 can be found in Fig. S6,
602 S7. GEMS generally places BMR city enhancements between $5 \times 10^{15} - 2 \times 10^{16}$ molecules cm⁻² in a N-S direction. Both
603 WRF_{Updated} D01, D02 generally reflect the spatial distribution and magnitude of tropospheric column NO₂ observed during
604 daylight hours. WRF_{Updated} D02 (Fig. 6b) tends to place the city plume more northward at 04:00:00 and 07:00:00 UTC
605 compared to what is observed in GEMS data (Fig 6a). This spatial discrepancy is likely related to overpredicted model winds
606 (further discussed in Sect. 6.1) which displaces the plume in a northward direction. Additionally, while the inversion
607 framework adjusts emission magnitudes temporally, it does not correct spatial errors in plume transport or source distribution
608 (See Sect. 7.2 for further discussion). Nevertheless, the daytime pattern seen in GEMS is accurately reflected in WRF_{Updated}
609 with column NO₂ values at their peak in the morning hours (08:00:00 LT), decreasing substantially throughout the afternoon
610 (14:00:00 LT) due to photochemical interactions. This is a substantial improvement from WRF_{Base}, which sees a large
611 overestimation of NO₂ in the morning hours followed by persistent and growing NO₂ columns throughout the afternoon as
612 seen in Fig. 6c.

613
614 The time series in Fig. 6d illustrates a full comparison of daytime tropospheric column NO₂ values across model types in D02
615 (see Fig. S7 for D01) for the duration of ASIA-AQ. WRF-GEMS_{Updated} indicates a clear reduction in error and bias from
616 WRF_{Base} as illustrated by the reduced NO₂ columns and model spread. WRF_{Updated} also indicates corrected daytime patterns
617 compared to WRF_{Base}, indicating better consistency with GEMS observations for the deployment period with few exceptions
618 such as 22 March where GEMS has peaks in the afternoon (further discussed in Sect. 6.1).



620 **Figure 6.** Spatial comparison over the BMR on 18 March 2024 of tropospheric NO₂ columns from (a) GEMS, (b) WRF-
621 GEMSU_{updated} D02, and (c) WRF-GEMSB_{Base} D02 for snapshots at 02:00:00, 04:00:00, and 07:00:00 UTC, corresponding to
622 approximately 09:00, 11:00:00, and 14:00:00 LT. (d) Tropospheric NO₂ column for daytime hours between GEMS (blue),
623 WRF-GEMSB_{Base} D02 (dotted purple), and WRF-GEMSU_{updated} D02 (solid purple) during the ASIA-AQ deployment period.
624 Shaded regions indicate variability, represented by the 10th and 90th percentiles.

625 **6 Evaluation using independent observations**

626 To independently assess the performance of the optimized WRF-Chem simulations, we compared three model configurations:
627 WRF_{Base}, WRF_{Updated}, and WRF_{Updated+BC} for D01 and D02 against a suite of independent airborne and ground-based
628 observations distinct from the satellite measurements used in the emission optimization process (see step 4 Fig. 2).
629 Comparisons between WRF_{Updated} and WRF_{Updated+BC} reflect the sensitivity of the model results to biases in the GEMS retrieval
630 used to constrain emissions in the optimization process. This evaluation primarily emphasizes the results of D02 (4 km), which
631 more directly represents urban-scale processes and exhibits improved performance compared to D01 across multiple
632 observational datasets. These datasets provide an unbiased test of how well the model reproduces meteorological conditions
633 and trace gas amounts beyond those directly constrained from GEMS observations. By evaluating WRF-Chem against surface
634 monitoring networks (Thailand PCD), Pandora spectrometer measurements, and airborne ASIA-AQ data (e.g., GCAS NO₂
635 columns, DC-8 vertical profiles), we examine the model's ability to capture daytime variability, vertical structure, and surface
636 concentrations of NO₂ across different spatial and temporal scales. Evaluation amongst these diverse datasets, therefore, helps
637 to support the robustness of the emission correction framework described in this paper.

638
639 **Table 2.** Summary of WRF-Chem D02 validation statistics for WRF_{Base} (B) WRF_{Updated} (U), and WRF_{Updated+BC} (U+BC)
640 simulations evaluated against independent observational datasets. Metrics include mean bias (MB), mean error (ME),
641 normalized mean bias (NMB), normalized mean error (NME), root-mean-square error (RMSE), and Pearson correlation
642 coefficient (CORR).

643
644
645
646
647
648
649
650
651

Dataset	Species	Model Run	MB	ME	NMB	NME	RMSE	CORR
GCAS	Tropospheric NO ₂ column (molecules cm ⁻²)	B	4.0E+15	5.1E+15	93	1.2E+2	9.3E+15	0.64
		U	-2.4E+14	1.9E+15	-5.6	45	3.4E+15	0.54
		U+BC	6.8E+14	2.3E+15	16	53	4.1E+15	0.4
DC-8	NO _x O ₃ NO ₂ (ppbV)	B	1.3	1.4	82	87	2.8	0.97
		U	-0.81	0.8	-49	49	1.4	0.93
		U+BC	-0.38	0.49	-23	30.3	0.89	0.94
	CANOE NO ₂ (ppbV)	B	1.4	1.5	87	94	2.9	0.97
		U	-0.76	0.76	-48	48	1.3	0.93
		U+BC	-0.34	0.50	-21	31	0.88	0.94
Ground Monitors	NO ₂ (ppbV)	B	12	12	1.3E+2	1.3E+2	15	0.61
		U	-3.0	4.5	-32	47	5.6	0.53
		U+BC	0.1	4.0	0.6	43	5.5	0.55
	NO _x (ppbV)	B	14	15	1.4E+2	1.4E+2	18	0.59
		U	-3.6	4.9	-34	47	6.7	0.61
		U+BC	0.02	4.8	0.2	46	7.1	0.57
	O ₃ (ppbV)	B	-5.6	8.2	-18	27	10	0.87

		U	4.9	8.5	16	27	11	0.81
		U+BC	3.1	6.6	10	22	9.2	0.86
Pandora	Tropospheric NO ₂ column (molecules cm ⁻²)	B	7.9E+15	8.6E+15	55	59	9.6E+15	0.71
		U	-6.6E+15	6.8E+15	-46	47	8.2E+15	0.67
		U+BC	-3.8E+15	4.9 E+15	-26	33	6.4 E+15	0.70

654

655 **6.1 Meteorological evaluation: winds and PBL height**

656 **6.1.1. Evaluation methodology**

657 To assess the performance of WRF-Chem meteorological fields, modeled wind speed and direction were evaluated against
658 surface observations across the BMR during the ASIA-AQ campaign, 14 – 27 March 2024. Biomass burning was active in the
659 region during the study period, particularly over northern Thailand and Myanmar, with peak activity occurring in mid-March.
660 However, transport to Bangkok was likely limited due to weak synoptic flow and short chemical lifetime of NO_x, reducing its
661 impact on urban concentrations of NO_x in the BMR. Following March 20, precipitation suppressed fire activity, further
662 minimizing its impact. While biomass burning may contribute to broader regional enhancements, its impact on the inversion
663 results and coincident model evaluation over Bangkok is expected to be minor.

664

665

666 Surface observations of wind speed (m s⁻¹) and direction are obtained from Thailand Pollution Control Department (PCD)
667 ground monitor network data. Hourly surface wind observations from PCD network data were co-located with corresponding
668 model outputs for D01 and D02. For each site, model data were extracted from the nearest grid cell and interpolated to
669 observation timestamps. Daily wind roses were constructed to visualize and compare the frequency distribution of wind speed
670 and direction between the model and observations. For each station, wind speeds were binned into intervals of 0-1, 1-3, 3-5,
671 and 5-8 m s⁻¹ and wind directions were grouped into 16 compass sectors. Normalized frequency counts were computed to
672 highlight dominant flow patterns. Data was averaged across stations within a larger bounding box around BMR, N-S (12.5-
673 15°N), W-E (99.5-101.5°E). For meteorology, we use a large box that spans the regional flow influencing Bangkok so that we
674 capture plume transport into and out of the city. Figure S8a illustrates the station locations and averaging domains in Bangkok.

675

676 Additionally, we performed an evaluation of planetary boundary layer height (PBLH) to gauge the model’s ability to capture
677 daily PBLH magnitude and development during the deployment period. Observed PBLHs were derived from the NASA
678 Langley airborne High Spectral Resolution Lidar Generation -2 (HSRL-2) data following a machine learning approach
679 described in Christopoulos et al., (2025) for ASIA-AQ flight days, 18 March, 19 March, 23 March, and 25 March 2024. We
680 evaluate PBLHs for aircraft raster periods (i.e., Raster 1: morning, Raster 2: afternoon, Raster 3: late afternoon/evening hours)
681 and co-locate the observed PBLHs to modeled PBLHs based on a nearest grid-cell approximation.
682

683 **6.1.2. Model-observation wind discrepancies**

684 Within the observational data, a pronounced synoptic transition occurred over Thailand on 20 – 21 March 2024, during which
685 winds reversed from the typical southwesterlies that were present during the deployment period to northeasterlies, weakened
686 substantially, coinciding with a drop in PBLH, and increased atmospheric stability (see observations; Fig. S9-10). This
687 transition played a major role in PM_{2.5} and ozone exceedances by promoting stagnation over the BMR. The WRF-Chem
688 simulation failed to capture the timing or strength of this abrupt wind shift and associated stagnation (Fig. S2a, S2b, S9b, S9c)).
689 The model instead maintained stronger southwesterly flow and higher PBLH, which led to unrealistic vertical mixing patterns
690 compared to the observations (Fig. S9-S10). Since this mismatch drives discrepancies between model and observations that
691 are unrelated to emissions adjustments/inversions, we exclude 20 – 21 March from the inversion/air quality evaluation.
692 Although the simulation is driven by FNL, it is possible for WRF-Chem to mis-time a rapid synoptic transition. This event
693 evolved on a relatively short spatial and temporal scale, and the coarse FNL boundary conditions may not have fully resolved
694 the sharp changes in low-level flow. In addition, local processes (i.e., convection, PBL mixing, land-sea interactions) around
695 Bangkok can cause the model to drift from the observed timing once it is integrated forward. We suspect these factors likely
696 contributed to the later wind shift in WRF-Chem. We additionally found WRF-Chem (D01, D02) systematically overpredicts
697 wind speed throughout the deployment (Fig. S2a, S2b; Table S2) with better agreement from the high-resolution 4 km domain.
698 This bias likely arises from the fact that many PCD monitors are embedded within the complex urban environment of Bangkok,
699 which are not fully resolved at WRF-Chem’s spatial scale.
700

701 The consequences of this mis-timed synoptic transition are most pronounced on 21 March as demonstrated in the next section,
702 when weak large-scale flow made the simulation highly sensitive to local processes. Under these conditions, WRF-Chem
703 misses the stagnation and dilutes pollutants too quickly. This helps explain why the model performs worst during the highest
704 observed PM_{2.5} and O₃ episode. These results indicate that forecast performance during similar weak-flow pollution events
705 would benefit from improved representation of urban boundary-layer processes (e.g., surface roughness, urban canopy effects,
706 and land–sea breeze structure).

707

708 **6.1.3. Model-observation PBLH discrepancies**

709 As shown in Fig. S10 and summarized in Table S3, WRF-Chem generally captures the temporal evolution of the PBLH
710 observed by the aircraft. During the daytime (afternoon hours represented by Raster 2-3), the simulated PBL is broadly
711 comparable to the observations, with median values that are often similar. However, the magnitude and sign of the model bias
712 vary by day, with WRF-Chem demonstrating both over- and under- estimation likely related to the meteorological conditions.
713 This day-to-day variability suggests PBLH biases are not systematic during the afternoon and may influence surface pollution
714 dilution differently across individual cases, potentially contributing to variability in simulated daytime NO₂ concentrations
715 rather than a consistent model bias.

716

717 **6.2 Surface air quality evaluation**

718 To evaluate model performance of surface trace gases, modeled surface mixing ratios of NO₂, NO_x, and O₃ were evaluated
719 against observations across BMR during 14 – 27 March 2024. Surface observations of these constituents (in ppbV) were
720 obtained from Thailand PCD ground monitor network data. Like the evaluation of wind speeds and direction, data was co-
721 located by extracting model information from the nearest grid cell and matched to the observation timesteps. Station data and
722 model data were averaged across stations located within the Bangkok urban plume, bounded by N-S (13.5-14.6°N), W-E
723 (100.2-101°E). Figure S8b illustrates the station locations and averaging domain in Bangkok. For the air quality evaluation,
724 we restrict the station averaging domain to a smaller area over the Bangkok urban plume. This smaller domain allows us to
725 assess how the inversion and optimization specifically correct the local plume structure as opposed to a broader regional
726 background.

727

728 **6.2.1. NO₂ and NO_x**

729 Figure 7a,7b,7c shows a comparison of average surface NO₂, NO_x, and O₃ (ppbV) for stations located within the Bangkok
730 urban plume during the ASIA-AQ deployment for D02. D01 results are available in Fig. S11. The 20 – 21 March is shaded in
731 grey to indicate the period where the model mis-represented synoptic conditions resulting in enhancements in the observed
732 concentrations due to stagnation. During this time, NO₂ and NO_x reached as high as 49, and 59 ppbV, respectively. O₃ peaked
733 at 103 ppbV the following day, on 22 March. Excluding this event, observed NO₂ and NO_x for this period generally ranged
734 between 3 – 17 ppbV, and 3.5 – 22 ppbV respectively. Overall, there is a clear improvement in the representation of NO₂ and
735 NO_x during this period in WRF_{Updated} and WRF_{Updated+BC} as shown in Fig 7a, 7b. Table 2 depicts summary statistics for this
736 analysis. The baseline simulation, WRF_{Base} overestimates both NO₂ and NO_x with mean biases of +12 ppbV and +14 ppbV,
737 respectively. With updated emissions, these large positive biases in WRF_{Updated} were eliminated and reversed, yielding mean

738 biases of -3.0 ppbV for NO₂ and -3.6 ppbV for NO_x. The remaining negative bias is likely linked to the overprediction of
739 winds, associated advection, and inversion related biases, which leads to locally diluted concentrations near urban sites as
740 shown in the previous analyses. WRF_{Updated+BC} further reduces the residual bias related to WRF_{Updated}, bringing mean biases
741 closer to zero (e.g., +0.1 ppbV for NO₂ and +0.02 ppbV for NO_x), while maintaining comparable error and correlation,
742 indicating accounting for the GEMS retrieval bias prior to inversion provides a modest additional improvement in model
743 performance. Correlations with observed NO₂ and NO_x remain moderate ($r = 0.5-0.6$) reflecting potential spatial discrepancies
744 in WRF_{Updated} as seen in the previous analyses. Average diurnal cycles of NO_x for D02, D01 are further illustrated in Fig. S12a,
745 c. Observed NO_x shows a clear morning peak and lower midday concentrations driven by boundary layer evolution. WRF_{Base}
746 overestimates NO_x and exaggerates the morning peak while WRF_{Updated} (dark purple) substantially improves both magnitude
747 and timing but underestimates the evening peak values. WRF_{Updated+BC} shows mixed performance with an overprediction of the
748 morning peak while the evening peak aligns more closely with observations compared to WRF_{Updated}, indicating a trade-off in
749 how the bias correction might redistribute NO_x across the diurnal cycle in the updated models.

750

751 6.2.2. O₃

752 Observed O₃ generally ranged between 14–57 ppbV, excluding the stagnation event on 20 – 21 March, and the baseline model
753 captures this range reasonably well (Fig. 7c). After updating the emissions, O₃ increases in WRF_{Updated} and WRF_{Updated+BC}
754 primarily at night, consistent with reduced NO titration following the decrease in NO_x emissions. Average diurnal cycles in
755 D02 (Fig. S12b,d) show that daytime O₃ production changes only modestly between base and updated simulations, indicating
756 the emission update mainly affects nighttime chemistry, as opposed to shifting photochemical O₃ formation in the daytime.
757 This pattern is reflected in the change in overall mean bias in Table 2, which shifts from an underprediction (-5.6 ppbV) to an
758 overprediction (+4.9 ppbV) in WRF_{Updated}. The overprediction is not as substantial in WRF_{Updated+BC} (+3.1 ppbV). While
759 WRF_{Updated} exhibits an earlier O₃ peak in D02 compared to observations, this shift is not present in D01 despite the same
760 emission inversion being applied. This likely suggests the discrepancy is driven by domain-dependent differences in
761 meteorological or chemical processes, rather than an error in the inferred NO_x emission timing. The O₃ peak is better
762 represented in WRF_{Updated+BC}.

763

764 The relatively weak daytime O₃ response to decreased NO_x emissions is consistent with recent analyses of O₃ formation
765 sensitivity during ASIA-AQ with in situ measurements, which indicate that the BMR exhibits mixed sensitivity to NO_x and
766 VOCs, in contrast to the predominantly NO_x-limited regimes observed at other ASIA-AQ locations (e.g., Manila) (Cho et al.,
767 2026). In this mixed-sensitivity regime, changes in NO_x emissions alone are not expected to strongly perturb daytime O₃
768 production, further providing validation for the minimal daytime O₃ response observed here. The magnitude of the daytime O₃
769 response varies by domain/model as shown by the D01 results (Fig. S12d). Although WRF_{Updated} D01 better matches observed
770 daytime O₃, this apparent improvement likely reflects NO_x titration associated with spatial dilution.

771

772 Overall, these results suggest that while the updated emissions improve the model's NO_x representation, further improvements
773 in VOC representation and local mixing processes may be needed to fully capture daytime O₃ levels in the BMR. Nevertheless,
774 the updated emissions substantially improve the model's simulation of surface NO₂ and NO_x, resulting in a more realistic
775 overall representation of air quality in Bangkok.

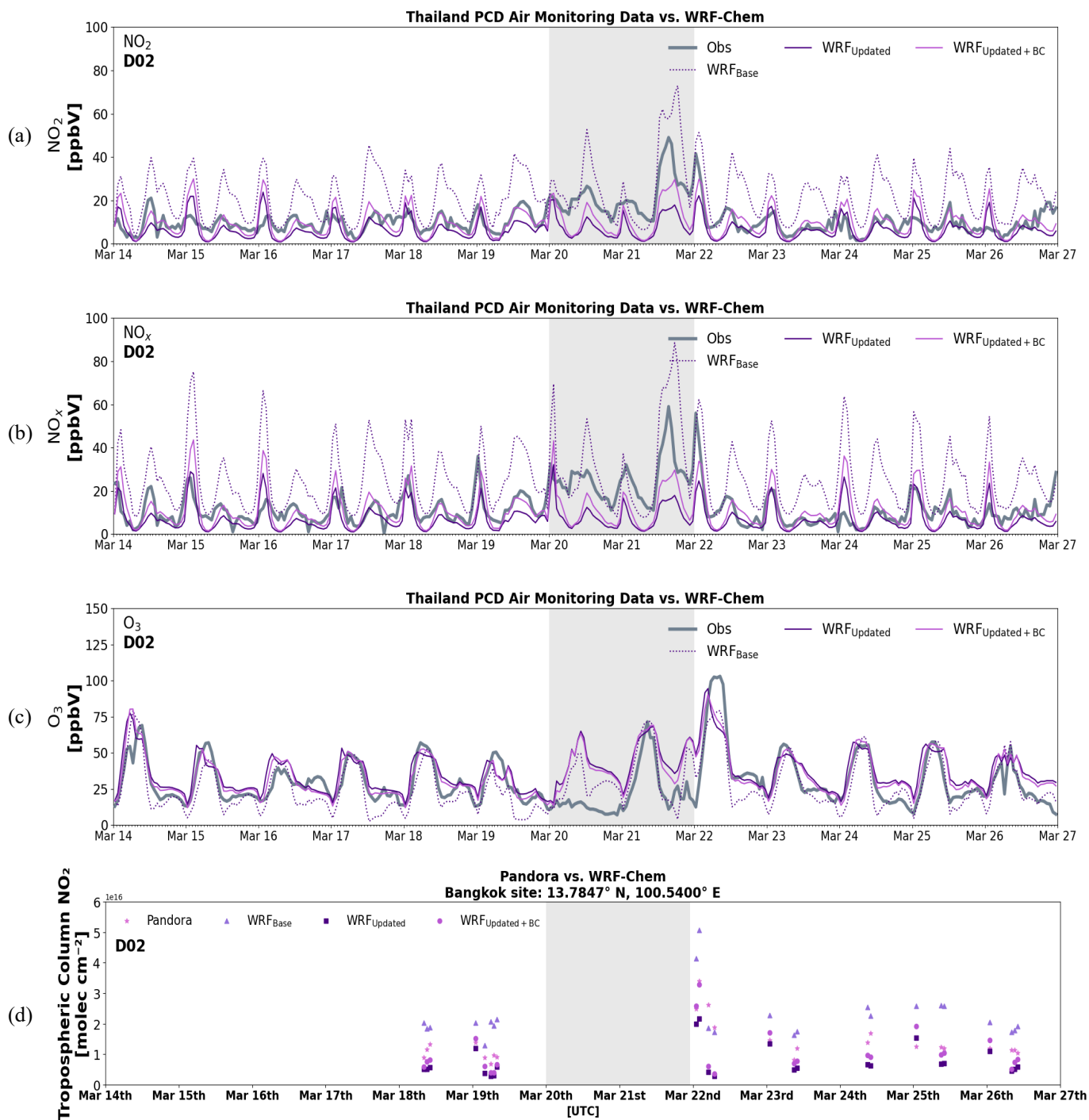
776

777 **6.3 Evaluation with Pandora column observations**

778 We additionally evaluate modeled NO₂ columns against Pandora measurements for the Bangkok site. Pandora NO₂ evaluation
779 used Level 2 direct-sun total column retrievals, filtered for high-quality measurements (quality flag = 10), and averaged to
780 hourly means. Tropospheric columns from Pandora were estimated by subtracting coincident or closest GEMS stratospheric
781 NO₂ at the nearest satellite pixel. Model columns were sampled at the nearest grid cell to the Pandora site and temporally
782 matched to observations.

783

784 Figure 7d depicts a comparison of WRF_{Base} (light purple triangles), WRF_{Updated} (dark purple squares), WRF_{Updated+BC} (magenta
785 dots) and Pandora (pink stars), tropospheric NO₂ column measurements for days with high quality data. Throughout this period,
786 Pandora measurements generally ranged between approximately $7 \times 10^{15} - 3.5 \times 10^{16}$ molecules cm⁻² and fit between WRF_{Base}
787 which places columns higher (e.g., up to 5×10^{16} molecules cm⁻²), WRF_{Updated+BC}, and WRF_{Updated} which places columns lower
788 (e.g. 2×10^{15} molecules cm⁻²). Average statistics between model cases for this analysis are shown in Table 2. Biases are
789 generally similar between model cases. WRF_{Base} overestimates column NO₂ as illustrated by the mean bias ($+7.9 \times 10^{15}$
790 molecules cm⁻²) whereas emissions updates contribute to an underestimation (-6.6×10^{15} molecules cm⁻²). However, there are
791 some improvements in absolute error metrics with ME and RMSE decreasing by roughly 20% and 12% respectively, and NME
792 dropping from 61% to 48%. The greatest bias improvements overall are seen in WRF_{Updated+BC} (-3.8×10^{15} molecules cm⁻²).
793 Figure S13 illustrates the spatial distribution of mean tropospheric model NO₂ bias for GEMS and Pandora during the time
794 reflected in Fig. 7d. In the WRF_{Base} simulation, a strong positive bias is seen within and north of the Pandora site, indicating
795 the overestimation of NO₂ columns (up to 2×10^{16} molecules cm⁻²) in the urban plume relative to GEMS. This pattern reiterates
796 the point that the prior anthropogenic emissions (based on EDGAR v5) were too large with pollutant accumulation occurring
797 downwind of Bangkok as a result. After applying the emission updates, the WRF_{Updated} simulation essentially eliminates this
798 bias. The overall bias near the Pandora site becomes close to neutral or slightly negative, demonstrating the optimization
799 effectively corrected the spatial overprediction. WRF_{Updated+BC} further reduces the residual negative bias relative to WRF_{Updated}
800 with NMB improving from -46% to -26% and RMSE decreasing from 8.2×10^{15} to 6.4×10^{15} molecules cm⁻². This indicates
801 that accounting for the GEMS retrieval bias in the initial optimization process partially corrects the remaining underestimation,
802 although some spatial discrepancies persist due to transport and plume placement error. Examples of daily biases for WRF_{Base}
803 D01, D02, and WRF_{Updated} D01, D02 can be found in Fig. S14 and Fig. S15.



804
805
806 **Figure 7.** Comparison of WRF_{Base} D02 (dotted purple), WRF_{Updated} D02 (solid purple), and WRF_{Updated+BC} D02 (solid magenta)
807 simulations against Thailand Pollution Control Department (PCD) ground-monitor network observations for (a) NO₂ mixing

808 ratio (ppbV), (b) NO_x mixing ratio (ppbV), and (c) O₃ mixing ratio (ppbV) during the ASIA-AQ deployment period (14 – 27
809 March 2024). represent averages across stations within the Bangkok urban plume. (d) Comparison of tropospheric NO₂
810 columns from WRF_{Base} D02 (light purple triangles), WRF_{Updated} D02 (dark purple squares), WRF_{Updated+BC} D01 (magenta dots)
811 and Pandora (pink stars) for high-quality observations during the ASIA-AQ deployment period (18 – 27 March 2024). The
812 shaded region represents the stagnation period, 20 – 21 March excluded from the evaluation.
813

814 **6.4 Evaluation with ASIA-AQ aircraft measurements**

815 The Airborne and Satellite Investigation of Asian Air Quality (ASIA-AQ) was a NASA field campaign conducted in February
816 – March 2024 to advance the understanding of urban and regional air quality across East and Southeast Asia. Targeting several
817 megacities (e.g., Manila, Seoul, Bangkok, Chiang Mai), the campaign combined satellite observations, aircraft measurements,
818 ground-based monitoring, and modeling approaches to characterize pollution sources and validate satellite retrievals. A main
819 objective of ASIA-AQ was to evaluate the data from GEMS. Airborne observations were collected using the NASA DC-8 in
820 situ and LaRC G-III remote sensing aircraft, with coordinated support from ground-based networks such as Pandora and
821 AERONET. Additionally, chemical transport models (e.g., GEOS-Chem, GEOS-FP, MUSICA, WRF-Chem, WRF-CMAQ)
822 played a key role in real-time flight planning and post-campaign interpretation.
823

824 **6.4.1. GCAS**

825 The GEOstationary Coastal and Air Pollution Events (GEO-CAPE) Airborne Simulator (GCAS) is an airborne UV-Vis
826 spectrometer that was flown on the G-III aircraft during the ASIA-AQ campaign. GCAS was designed to simulate the
827 spectral capabilities of TEMPO and GEMS, but with a much finer pixel resolution of approximately 250 x 560 m at flight
828 altitude (Janz et al., 2019; Lee et al., 2024). GCAS uses a push-broom remote sensing technique and consists of two
829 spectrometer channels: a UV-Vis channel (300-490 nm) optimized for air quality measurements, and a Vis-NIR channel (480-
830 900 nm) for ocean color observations (Kowalewski and Janz, 2014; Lee et al., 2024). This work focuses on the NO₂ retrieval
831 from spectra in the UV-Vis channel. Retrieval details and validation results can be found in Judd et al., (2020) but were
832 previously found to be unbiased with uncertainties within +/-25%. As in previous field campaigns, the aircraft executed a
833 “lawnmower” flight pattern with parallel flight lines spaced 6.3 km apart, providing about 10% overlap between flight lines
834 assuming a flight altitude of 28,000 feet. This flight strategy, combined with the instrument’s 45° field of view, allowed for
835 the generation of gap-free NO₂ column maps up to three times per day, period referred to as a “raster”. Due to the short duration
836 of each raster period (~3 hours), local meteorological conditions often influence the fine-scale structures observed in the GCAS
837 NO₂ data (Goldberg et al., 2024). Here, we evaluate the WRF-Chem runs against GCAS for several flight days: 18 March, 19
838 March, 23 March, and 25 March 2024.
839

840 We perform the evaluation for each raster separately to isolate specific flight patterns and accurately evaluate spatial gradients
841 in NO₂ between the model and observations. For each analysis, GCAS pixels corresponding to the flagged raster were retained
842 for comparison. Additional filters were applied to remove poor-quality retrievals. We masked pixels with cloud or sun glint
843 contamination based on a provided flag variable (`cloud_glint_flag = 1`) and discarded retrievals with missing data or undefined
844 AMFs. GCAS provides separate NO₂ vertical columns above and below the aircraft, as well as model-derived scattering
845 weights, and AMFs for both portions. The above and below aircraft contributions can be approximated as the stratospheric
846 and tropospheric contributions, respectively. For this evaluation, we focus exclusively on the NO₂ column below the aircraft
847 or the tropospheric column NO₂, which is the portion most relevant to surface-level air quality and most comparable to our
848 WRF-Chem results. We compute the below-aircraft averaging kernel, A_i^{below} , as:

849
$$A_i^{below} = \frac{SW_i}{AMF_{below}} (17)$$

850 Here, SW_i represents the scattering weight for layer i , representing the sensitivity of the measured radiance to NO₂ in that
851 layer. This averaging kernel represents the satellite-equivalent vertical sensitivity to NO₂ below the aircraft and was used to
852 weigh the WRF-Chem vertical profile.

853

854 WRF-Chem output including, NO₂ mixing ratio, pressure, temperature, and height were used to compute air density and
855 convert volume mixing ratios to number densities as previously done in the GEMS evaluation. Each GCAS pixel was
856 temporally matched to the nearest model output time (rounded to nearest hour) and spatially co-located by finding the nearest
857 WRF-Chem grid cell. To isolate the portion of the model column below the aircraft, we filtered the model levels based on the
858 aircraft altitude reported at each pixel. We compute the tropospheric column as shown in Eq. (10). To generate a model column
859 that reflects the vertical sensitivity of the GCAS retrieval, we interpolate the WRF-Chem profile to the number of GCAS
860 vertical layers (49), converted the mixing ratios to number density, and applied the GCAS averaging kernel to yield WRF-
861 GCAS.

862

863 The maps in Fig. 8 illustrate a spatial comparison between (a) GCAS, (b) WRF-GCAS_{Updated+BC} D02, (c) WRF-GCAS_{Updated}
864 D02, and (d) WRF-GCAS_{Base} D02 over BMR for a flight day on 18 March 2024. D01 spatial comparisons are available in Fig.
865 S16. 18 March represents a typical example of local pollution dominating BMR with minimal influences from long-range
866 pollution transport and biomass burning. The GCAS instrument generally places tropospheric column NO₂ values in BMR
867 between $5 \times 10^{15} - 2 \times 10^{16}$ molecules cm⁻², with the largest enhancements observed in the city center, as also seen in the
868 GEMS data (Fig. 7). A clear N-S plume is visible in the data, reflecting persistent southerly onshore flow from the Gulf of
869 Thailand. This pattern coincides with the seasonal shift from the northeast to southwest monsoon. Overall, WRF-GCAS_{Updated}
870 and WRF-GCAS_{Updated+BC} generally better capture the spatial differences and magnitudes of tropospheric column NO₂ in BMR
871 for different raster periods compared to WRF-GCAS_{Base}. WRF_{Updated+BC} outperforms WRF_{Updated} in capturing NO₂ column
872 enhancements, particularly during raster 2 (late morning – afternoon LT). GCAS also illustrates enhanced NO₂ columns

873 southeast of Bangkok in a region known as the Eastern Economic Corridor (EEC), a major hub for industrial activity (e.g.,
874 automotive manufacturing, petrochemicals, electronics). WRF_{Updated}, WRF_{Updated+BC}, and WRF_{Base} tend to underestimate
875 pollution levels in the EEC. This is likely related to wind speed overprediction and a lack of updated regional source data in
876 the EDGAR v5 inventory (since this is a region outside of the performed inversion). Information from a local emissions
877 inventory, or additional inversions performed on this region could aid the model in better representing the air quality in this
878 region, which has similar magnitudes of column NO₂ (2×10^{16} molecules cm⁻²) to the Bangkok city center.

879
880 Statistics for this analysis are shown in Table 2. Overall, statistics are representative of substantial bias and error improvements
881 in the updated runs from WRF_{Base}, which significantly overpredicts column NO₂ amounts in the region for all raster periods.
882 For example, ME and RMSE are improved by ~62% from WRF_{Base} and WRF_{Updated}. Mean biases are negative which indicate
883 WRF_{Updated} is underpredicting NO₂ columns. This is likely the result of the low inversion biases and windspeed overprediction.
884 However, this underprediction is improved throughout the day as seen in Fig. S17a, S17b. This is in opposition to WRF_{Base},
885 which increases in biases and error for each raster as also shown in Fig. S17a, S17b. These daytime patterns also highlight an
886 important distinction between the benefits of geostationary (GEMS) versus LEO observations. Morning improvements are
887 particularly strong because the inversion directly constrains the rapid rise in emissions during the morning, something that
888 LEO sensors generally under sample due to their limited overpass frequency. Midday and afternoon performance remains
889 improved as well, but the morning hours show the clearest advantage of daytime GEO sampling for capturing short-timescale
890 emission variability. Similar results are demonstrated in WRF_{Updated} D01 (Fig. S18). WRF_{Updated+BC} is indicative of a partial
891 correction to the negative bias in WRF_{Updated}, shifting the NMB from -5.6% to +16%. While this brings the simulated NO₂
892 columns closer to observations in a mean sense, is it followed by increases in error, suggesting a trade-off between bias
893 reduction and overall model performance.

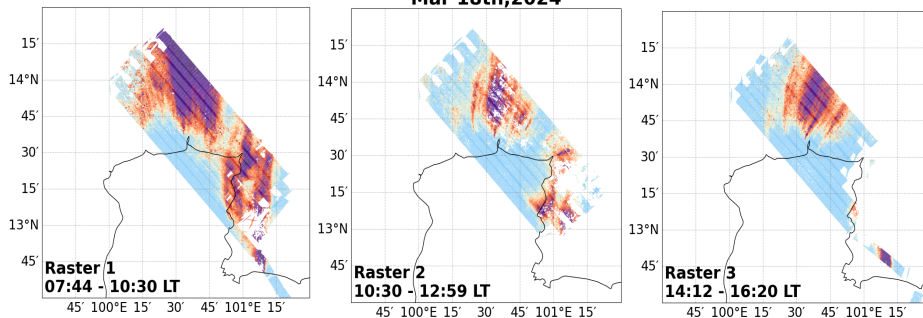
894
895 Correlations remain moderate (0.4 – 0.6) for model cases, however, WRF_{Updated} and WRF_{Updated+BC} illustrate weaker correlations
896 likely due to (i) subtle shifts in the urban plume placement (i.e., shift in a more northerly direction), and (ii) a reduction in
897 dynamic range after emissions corrections. For example, when plume magnitudes are lowered, the variability shrinks allowing
898 the correlations to become less sensitive to spatial-temporal agreement and more sensitive to small plume-placement
899 differences as is the case here.

900

Mar 18th, 2024

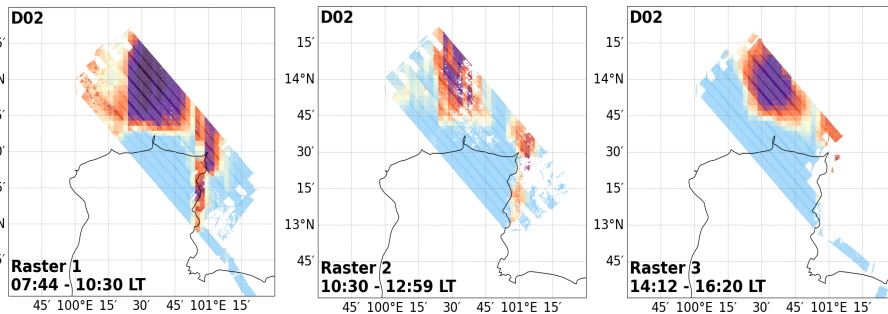
(a)

GCAS



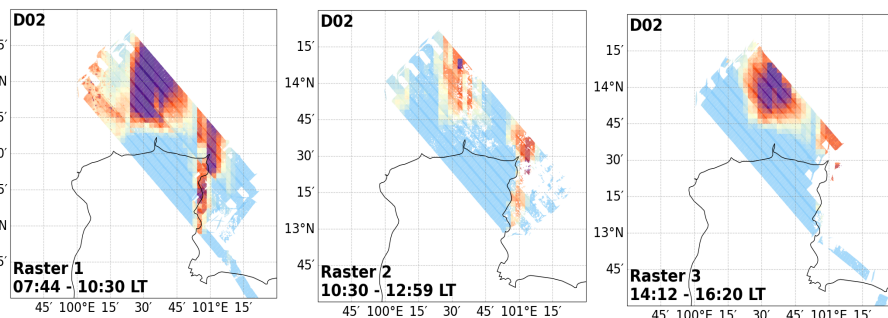
(b)

WRF-GCAS^{Updated + BC}



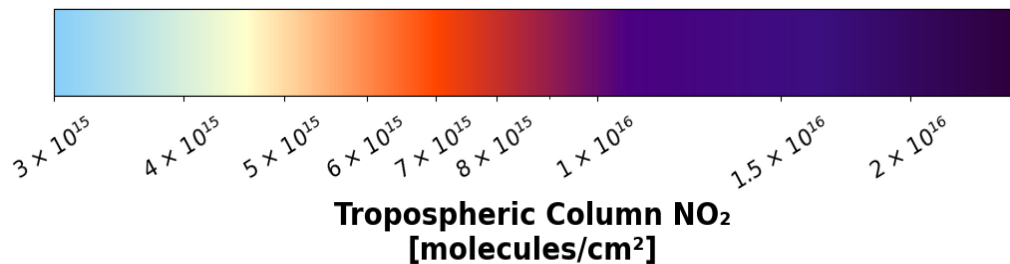
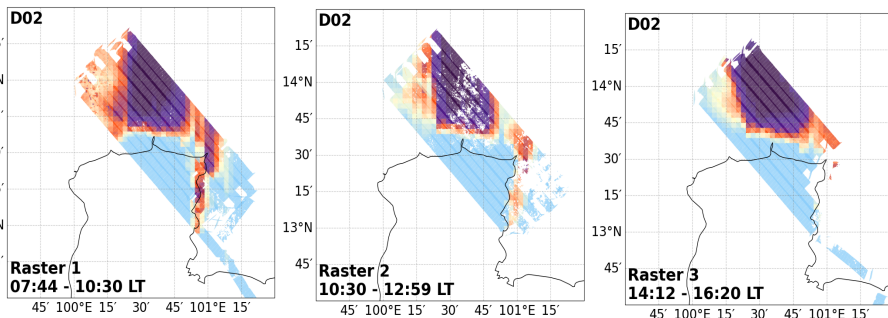
(c)

WRF-GCAS^{Updated}



(d)

WRF-GCAS^{Base}



902

903 **Figure 8.** Spatial comparison over the BMR on 18 March 2024 of tropospheric NO₂ columns from (a) GCAS, (b) WRF-
904 GCAS_{Updated+BC} D02, (c) WRF-GCAS_{Updated} D02 and (d) WRF-GCAS_{Base} D02 for raster periods corresponding to morning,
905 afternoon, and early evening local time.

906 **6.4.2. NO_xO₃ and CANOE (DC-8)**

907 We additionally compare the model simulations to in situ NO₂ data gathered by the National Center for Atmospheric
908 Research's (NCAR) NO_xO₃ and NASA's GSFC's Compact Airborne NO₂ Instrument (CANOE) aboard the DC-8 aircraft. The
909 NO_xO₃ instrument is a 3-channel chemiluminescence instrument designed for the measurement of NO, NO₂, and O₃ (Ridley
910 et al., 1992; Ridley and Grahek, 1990). CANOE measures NO₂ using non-resonant laser induced fluorescence (LIF) (St. Clair
911 et al., 2019). We use the 1-sec DC-8 data for the flights conducted in Thailand during March 2024 (18 March, 25 March).
912 A visual depiction of the DC-8 flight path is shown in Fig. S19. The typical flight path included several low-altitude
913 descents/ascents over several airports (see Fig. S19b) along with long-distance transects across Central Thailand.

914

915 To evaluate model performance, we match hourly WRF-Chem outputs from both the 20 km (D01) and 4 km (D02) domains
916 to the aircraft location and time. For each observation, we extract co-located model NO₂ values along the aircraft track. Profiles
917 are filtered by location (e.g., Don Mueang International Airport in Bangkok) and direction (e.g., ascent or descent) using flags
918 in the provided observational datasets. Individual profiles are grouped by their unique number, and we bin the observations
919 and model output by altitude (50 m vertical bins). For each bin, we compute mean NO₂ from the aircraft and model datasets.
920 These vertically resolved comparisons allow us to assess model skill in capturing the observed structure and magnitude of NO₂
921 within the boundary layer and lower troposphere.

922

923 Figure 9 depicts a comparison of aggregated in situ NO₂ vertical profiles over the Don Mueang International airport for (a) 18
924 March and (b) 25 March. Model scenarios are shown in shades of purple (WRF_{Base}: dotted dark purple; WRF_{Updated}: solid dark
925 purple; WRF_{Updated+BC} solid magenta), and in situ information from two instruments aboard the DC-8, NO_xO₃ (solid) and
926 CANOE (dashed) are displayed in black. The location of the Don Mueang International Airport with respect to the Bangkok
927 urban plume is depicted in (c). We separate and group the data by time of day to gauge how the model runs perform with
928 respect to time of day. Corresponding plots for D01 are available in Fig. S20. As shown in Fig. 9, the NO_xO₃ and CANOE
929 NO₂ measurements exhibit excellent agreement throughout the analysis period. This consistency between two independent in
930 situ instruments strengthens confidence in the observational data used for model evaluation. Comparison with DC-8 in situ
931 NO₂ profiles show that WRF_{Base} consistently overestimated observed concentrations, with a mean bias of +1.3 ppb and
932 normalized mean bias near 80%. Figure 9a and Figure 9b indicate the overestimation is most pronounced near the surface
933 during the morning, where WRF_{Base} exceeds observations by nearly 25 ppb. WRF_{Updated+BC} also suggests an overestimation
934 compared to aircraft observations in the morning. In contrast, WRF_{Updated} captures the observed morning surface enhancements

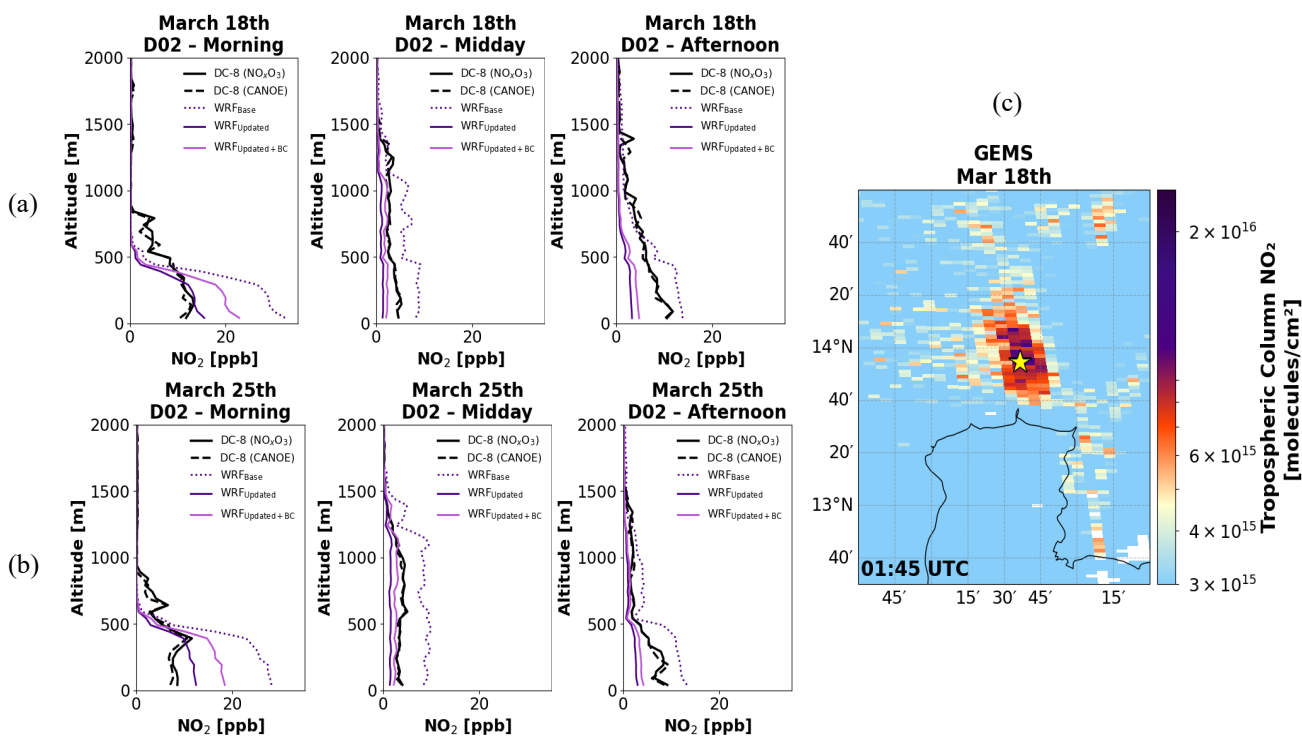
935 accurately. As time progresses, however, WRF_{Updated} and WRF_{Updated+BC} begin to underestimate the column (average bias ~ -
 936 0.3 to -0.8 ppb), though both mean error and RMSE remain improved in the updated cases relative to WRF_{Base} (Table 2). This
 937 daytime behavior likely reflects the nature of the GEMS-based emission constraints, which are directly applied only until
 938 14:00:00 LT, after which a single daily scaling factor is applied on the input emissions. As afternoon PBL growth and
 939 photochemistry evolve, the fixed scaling likely results in an underestimation in the afternoon profiles. Additionally,
 940 overestimated model winds speeds may further dilute surface concentrations, likely contributing to the midday and afternoon
 941 biases shown in WRF_{Updated}, and WRF_{Updated+BC}. The afternoon underestimation is slightly reduced in WRF_{Updated+BC}, likely
 942 reflecting the impact of the bias correction applied prior to inversion/NO_x emission optimization.

943

944 Correlations for WRF_{Updated} ($r = 0.93 - 0.97$) and WRF_{Updated+BC} ($r = 0.94$) remain high indicating the simulation preserved the
 945 observed structure while improving the overprediction. Overall, these results highlight the effectiveness of the emission
 946 updates in accurately capturing morning surface air quality. This suggests that while the updated emissions substantially
 947 improve the magnitude of modeled NO₂, remaining discrepancies are driven primarily by meteorological transport rather than
 948 emission magnitude.

949

950



951

952

953 **Figure 9.** Comparison of WRF-Chem D02 simulations (WRF_{Base}: dotted dark purple; WRF_{Updated}: solid dark purple;
954 WRF_{Updated+BC}: solid magenta) with airborne in situ measurements from the CANOE (dashed black) and NO_xO₃ (solid black)
955 instruments aboard the DC-8 for (a) 18 March and (b) 25 March 2024. Profiles are grouped by morning (06:00:00–11:00:00
956 LT), midday (11:00:00–13:00:00 LT), and afternoon (13:00:00–17:00:00 LT) approaches at Don Mueang International Airport
957 in northern Bangkok, whose location relative to the Bangkok urban plume is shown within a GEMS snapshot in (c).
958

959 7 Discussion

960 7.1 Implications of GEMS NO₂ retrieval biases

961 In our study, the comparisons with independent aircraft and ground-based observations indicate the satellite-constrained
962 emissions without bias-corrections presented here may represent a low estimate. In particular, the systematic low bias in GEMS
963 NO₂ is consistent with the negative biases often seen in the WRF_{Updated} simulations. Importantly, this bias could not be
964 diagnosed using the satellite data alone.

965 To further evaluate the relative behavior of GEMS and airborne GCAS NO₂ columns, we compare their tropospheric columns
966 using WRF_{Updated+BC} as a common transfer framework (Fig. S21). Figure S21 compares the observed GCAS/GEMS NO₂
967 column ratios with ratios calculated after both datasets are mapped through WRF_{Updated+BC}. In the observations, GCAS columns
968 are consistently higher than the raw GEMS columns as illustrated by the orange line, with GCAS/GEMS ratios of ~2–3 on
969 most days and values reaching ~6–7 on 21 March. In contrast, the corresponding WRF-GCAS_{Updated+BC}/WRF-GEMS_{Updated+BC}
970 ratios are closer to 1:1 (~1.1–1.7), even on 21 March. This behavior is consistent with a low bias in GEMS NO₂ columns
971 relative to GCAS. After applying the bias correction, the GCAS/GEMS_{BC} ratios approach 1:1 on most days, indicating
972 improved consistency between the datasets, and supporting the effectiveness of the applied GEMS bias correction.

973 When incorporating bias-corrected retrievals into the top-down inversions and NO_x emission optimization process, the
974 resulting WRF_{Updated+BC} run reduces the negative biases in the independent validation, in some cases bringing the model results
975 even closer to observations as seen in the surface air quality analysis. However, this improvement is not uniform. In certain
976 comparisons (e.g., GCAS and DC-8), WRF_{Updated+BC} introduces a tendency toward overprediction in morning hours,
977 highlighting tradeoffs associated with the bias correction. These results suggest that while accounting for the retrieval bias can
978 improve mean model performance, additional uncertainties such as overestimated wind speeds and associated transport errors
979 continue to influence the representation of modeled NO₂.

980 Here, the integration of ground-based, airborne, satellite, and model data provides a powerful framework not only for
981 improving emissions but also for identifying limitations within individual observing systems. While WRF_{Updated} clearly

982 outperforms the baseline model, and WRF_{Updated+BC} offers targeted improvements in reducing systematic bias, the combined
983 observational evidence highlights the necessity of a multi-platform validation to fully interpret the satellite-based emission
984 estimates.

985 Despite this low bias in the GEMS retrieval, the high-frequency daytime sampling provided by geostationary observations
986 offers critical constraints on daytime variability and plume evolution that are particularly valuable for emission inversion and
987 air quality modelling. For example, the GEMS-constrained emission adjustments presented here were critical for improving
988 the temporal evolution of NO_x in WRF-Chem, resulting in substantial and robust improvements in model performance across
989 independent evaluations. Future work may further benefit from continued refinement of bias-corrected GEMS products and
990 upcoming algorithm improvements (e.g., v4), alongside improved representation of spatial representation of emissions within
991 the model.

992

993 **7.2 Limitations and potential extensions of the inversion framework**

994 The current model emission update framework optimizes the temporal evolution of emissions but does not explicitly resolve
995 regional variability, as a single set of hourly scaling factors is applied uniformly across all grid cells within the BMR. As a
996 result, the inversion preserves the spatial structure of the prior inventory, and any inaccuracies in the spatial distribution of
997 emissions are not corrected.

998

999 Extending this approach to resolve emissions at finer scales would require allowing emissions to vary across grid cells or
1000 subregions, supported by additional constraints. These constraints could include regional higher-resolution regional prior
1001 inventories when available, as well as higher-resolution observations (e.g., GCAS) that can better resolve the urban variability
1002 in NO₂ as shown in this analysis.

1003 **8 Conclusion and Discussion**

1004 **8.1 A GEO-constrained framework for anthropogenic NO_x emissions**

1005 Accurate urban NO_x emissions remain a major challenge for air quality modeling efforts, but geostationary satellites now offer
1006 a path forward. This work takes a novel approach in improving urban NO_x emissions using daytime GEO satellite observations.
1007 We quantify and reduce biases in modeled NO₂ over the Bangkok Metropolitan Region (BMR), by integrating GEMS
1008 constraints into a high-resolution model's daytime prior emission profile. We first used top-down inversions of hourly GEMS
1009 NO₂ columns with the Cross-Sectional Flux (CSF) method to develop an average daytime NO_x profile for the BMR in March
1010 2024. Using this information, we developed and applied an optimization framework that incorporates physical constraints (i.e.,

1011 with regards to emissions accumulation and lifetime) to reshape the WRF-Chem's daytime emission pattern and magnitude to
1012 better reflect observed emissions variability in the BMR.

1013
1014 This represents one of the first applications of the *ddeg* framework to estimate hourly urban NO_x emissions with geostationary
1015 observations in Southeast Asia. In contrast to a full chemical reanalysis, the *ddeg*-based framework provides an efficient and
1016 scalable alternative that does not require repeated model reinitialization of extensive chemical state optimization. This makes
1017 the approach particularly suitable for regional applications and for broader application across different modeling systems and
1018 urban environments within the domain of GEO sensors.

1020 **8.2 Model improvements across independent observational platforms**

1021 Re-running WRF-Chem (D01 – 20 km; D02 – 4 km) with an updated NO_x emission profile (WRF_{Updated}; WRF_{Updated+BC}) led to
1022 substantial improvements across multiple independent datasets. Model evaluation with ground monitors, Pandora, GCAS, and
1023 DC-8 observations consistently showed reduced biases and errors relative to the baseline simulation based on EDHAR v5
1024 emissions. For example, surface-level comparisons with Thailand PCD ground network data confirmed some of these trends
1025 in WRF_{Updated}, with mean biases in NO₂ and NO_x decreasing from +12 - +14 ppbV in WRF_{Base} to roughly -3 ppbV in WRF_{Updated},
1026 and 0.02 to 0.1 ppbV in WRF_{Updated+BC}. At the Bangkok Pandora site, mean bias shifted from strongly positive ($+7.9 \times 10^{15}$
1027 molecules cm⁻²) to negative, and normalized mean errors decreased by ~20-4% in WRF_{Updated} and WRF_{Updated+BC}. Evaluation
1028 against GCAS airborne column retrievals further showed that the emissions updates improved spatial variability and magnitude
1029 of NO₂ across the Bangkok urban plume, reducing mean and root mean square errors by ~55-63% in WRF_{Updated} and
1030 WRF_{Updated+BC} compared to WRF_{Base}. The DC-8 in situ vertical profiles further illustrated that WRF_{Updated} could substantially
1031 reduce near-surface overestimation in morning hours and preserve the observed vertical structure of NO₂ mixing ratios.

1033 **8.3 Assessing GEMS bias through multi-platform integration**

1034 Overall, these results demonstrate that incorporating geostationary satellite constraints into regional, high-resolution (4 km)
1035 chemical transport models can substantially improve the representation of urban air quality over Bangkok. Large biases in the
1036 baseline simulation are likely driven by reliance on outdated global emissions inventories (e.g., EDGAR v5), which do not
1037 reflect recent changes in regional anthropogenic activity, as well as uncertainties in bottom-up methodologies where updated
1038 local estimates appear systematically high. The satellite-constrained emission estimates derived here are consistent with
1039 independent top-down approaches (e.g., TCR-3) based on different satellite platforms and methodologies, increasing
1040 confidence in the inferred reductions.

1041 Comparisons with independent aircraft and ground-based observations further indicate that the GEMS-constrained emissions
1042 presented here may represent an underestimate. In particular, the systematic low bias reported for the GEMS v3 NO₂ product
1043 is consistent with the remaining negative biases observed in WRF_{Updated}. By accounting for this bias through the application of
1044 bias-corrected retrievals, WRF_{Updated+BC} reduces these negative biases, although in some cases introduces a tendency toward
1045 overprediction, highlighting tradeoffs associated with the correction. While model output (e.g., WRF_{Base}) can serve as a transfer
1046 standard for comparing different observing systems, these results highlight the importance of integrating ground-based,
1047 airborne, satellite, and model information to robustly identify biases and improve emission estimates.

1048 **8.4 Value of hourly GEO constraints, high-resolution modelling and future directions**

1049 A key strength of this framework is the use of hourly daytime constraints uniquely provided by geostationary observations,
1050 which enable direct characterization of daytime emission variability and plume evolution that cannot be captured by once-
1051 daily low-Earth-orbit measurements. These daytime constraints are particularly important for urban environments, where
1052 emissions, chemistry, and boundary-layer dynamics vary rapidly and strongly influence air quality impacts.

1053 Coarse (~12 km) simulations have been shown to inadequately represent circulations in coastal environments, and nonlinear
1054 NO_x chemistry, leading to systematic biases in simulations of NO₂ (Hsu et al., 2026; Valin et al., 2011; Verreyken et al., 2025;
1055 Yu et al., 2023). These limitations in model resolution are expected in coastal megacities such as Bangkok with complex local
1056 topography and land-sea contrasts. Consistent with recent TEMPO-based emission studies indicating that model resolution
1057 can limit the robustness of GEO-based top-down NO_x constraints (Hsu et al., 2026), these considerations motivate the use of
1058 4 km WRF-Chem simulations in this work as a necessary framework for accurately interpreting geostationary satellite
1059 observations and constraining urban NO_x emissions.

1060 While remaining discrepancies, including the negative model biases, are likely influenced in part by overpredicted model wind
1061 speeds and associated transport errors, future work could benefit from finer-resolution simulations (< 4 km) and more
1062 advanced urban parameterizations (e.g., multi-layer urban canopy models; Liu et al., (2025)) to better represent urban flow,
1063 drag, and mixing. Continued validation and further development of bias-corrected for updated GEMS retrievals will also
1064 strengthen the use of geostationary NO₂ products. Nevertheless, the high-frequency daytime sampling provided by GEMS
1065 already offers critical information for emission inversion, and the integration of GEMS-derived constraints into WRF-Chem
1066 represents a scalable pathway toward near-real-time, satellite-informed emissions estimation and improved air quality
1067 forecasting for rapidly developing megacities.

1068 **Code Availability.**

1069 The code repository for *ddeq v1* is available on GitLab: <https://gitlab.com/empa503/remote-sensing/ddeq>, Kuhlmann, 2024a.
1070 The implementation of *ddeq v1* for top-down NO_x estimates and model optimization scripts are publicly available via Zenodo
1071 (<https://doi.org/10.5281/zenodo.18381169>).

1072 **Data Availability.**

1073 All ASIA-AQ field campaign data used in this study (i.e., GEMS NO₂ v3, NO_{xy}O₃, CANOE, GCAS, Thailand PCD air quality
1074 monitoring data) are openly available and were acquired from their NASA Langley Research Center maintained archive:
1075 <https://www-air.larc.nasa.gov/cgi-bin/ArcView/asiaaq>. Pandora total column NO₂ observations are available through the
1076 Pandonia Global Network website: <https://www.pandonia-global-network.org/home/documents/pgn-data/>. ERA5
1077 meteorological reanalysis data were obtained from the Copernicus Climate Data Store: <https://cds.climate.copernicus.eu/>.
1078 Global emissions used in this study are openly available as well, HTAP v3.2 (https://edgar.jrc.ec.europa.eu/dataset_htap_v32),
1079 MIXv3.1(<https://csl.noaa.gov/groups/csl4/modeldata/data/Li2023/>), EDGARv5(https://edgar.jrc.ec.europa.eu/dataset_ghg50),
1080 ODIAC (<https://db.cger.nies.go.jp/dataset/ODIAC/>). THAI-KMUTT, and TCR-3 emissions can be made available upon
1081 request.

1082 **Supplement.**

1083 The supplement related to this article is available online.

1084 **Author Contributions**

1085 JAC designed the study, performed the model simulations, conducted the data analysis, prepared all figures, and wrote the
1086 initial draft of the manuscript. PS supervised the project, contributed ideas, guidance, and discussions regarding the model

1087 framework and interpretation of results. MM provided additional guidance on the modeling framework and interpretation of
1088 results. All authors discussed the results and contributed to the final version of the manuscript.

1089 **Competing Interests**

1090 At least one of the (co-)authors is a member of the editorial board of Atmospheric Chemistry and Physics.

1091 **Acknowledgements**

1092 We thank the entire ASIA-AQ team for their contributions to the field experiment. We extend our gratitude to the instrument
1093 teams for their efforts in conducting in situ measurements, to the airborne remote sensing teams (HSRL-2 and GCAS) for their
1094 data collection and support, and the GEMS team for providing the data utilized in this work. The TCR-3 product was generated
1095 by calculations using the Earth Simulator with the support of the Japan Agency for Marine-Earth Science and Technology.

1096 **Financial Support**

1097 The funding for this research came from the National Aeronautics and Space Administration under awards 80NSSC22M0266
1098 and 80NSSC23K0786. Additionally, part of this work was carried out at the Jet Propulsion Laboratory, California Institute of
1099 Technology, under contract to NASA (80NM0018D0004). The views expressed in this manuscript are those of the authors
1100 and do not reflect the views of NASA.

1101 **References**

1102
1103 Agarwal, P., Stevenson, D. S., and Heal, M. R.: Evaluation of WRF-Chem-simulated meteorology and aerosols over northern
1104 India during the severe pollution episode of 2016, *Atmospheric Chemistry and Physics*, 24, 2239–2266,
1105 <https://doi.org/10.5194/acp-24-2239-2024>, 2024.

1106 Ahmadov, R., McKeen, S. A., Robinson, A. L., Bahreini, R., Middlebrook, A. M., Gouw, J. A. de, Meagher, J., Hsie, E.-Y.,
1107 Edgerton, E., Shaw, S., and Trainer, M.: A volatility basis set model for summertime secondary organic aerosols over the
1108 eastern United States in 2006, <https://doi.org/10.1029/2011JD016831>, 2012.

1109 Anav, A., Sorrentino, B., Collalti, A., Paoletti, E., Sicard, P., Coulibaly, F., Manzini, J., Hoshika, Y., and De Marco, A.:
1110 Meteorological, chemical and biological evaluation of the coupled chemistry-climate WRF-Chem model from regional to
1111 urban scale. An impact-oriented application for human health, *Environmental Research*, 257, 119401,
1112 <https://doi.org/10.1016/j.envres.2024.119401>, 2024.

1113 Anenberg, S. C., Mohegh, A., Goldberg, D. L., Kerr, G. H., Brauer, M., Burkart, K., Hystad, P., Larkin, A., Wozniak, S., and
1114 Lamsal, L.: Long-term trends in urban NO₂ concentrations and associated paediatric asthma incidence: estimates from global
1115 datasets, *The Lancet Planetary Health*, 6, e49–e58, [https://doi.org/10.1016/S2542-5196\(21\)00255-2](https://doi.org/10.1016/S2542-5196(21)00255-2), 2022.

1116 ASIA-AQ White Paper | ASIA-AQ: https://espo.nasa.gov/asia-aq/document/ASIA-AQ_White_Paper, last access: 6 January
1117 2025.

1118 `minimize(method='SLSQP')` — SciPy v1.16.2 Manual: [https://docs.scipy.org/doc/scipy/reference/optimize.minimize-](https://docs.scipy.org/doc/scipy/reference/optimize.minimize-slsqp.html)
1119 `slsqp.html`, last access: 4 November 2025.

1120 Aung, S. H., Gheewala, S. H., Winijkul, E., Panyametheekul, S., and Prapasongsa, T.: Environmental impacts and costs of
1121 ozone formation in Bangkok Metropolitan Region, *Atmospheric Pollution Research*, 16, 102450,
1122 <https://doi.org/10.1016/j.apr.2025.102450>, 2025.

1123 Bae, K., Richter, A., Lange, K., Friedrich, M. M., Pinaridi, G., Roozendaal, M. V., Merlaud, A., Fayt, C., Bösch, T., Zilker, B.,
1124 Latsch, M., Behrens, L. K., Lee, H., Jung, Y., Hong, H., Chang, L.-S., and Song, C.-K.: Comparison of GEMS v3.0
1125 tropospheric NO₂ columns with ground-based DOAS instruments in Ulsan, *GIScience & Remote Sensing*, 2025.

1126 Beirle, S., Boersma, K. F., Platt, U., Lawrence, M. G., and Wagner, T.: Megacity Emissions and Lifetimes of Nitrogen Oxides
1127 Probed from Space, *Science*, 333, 1737–1739, <https://doi.org/10.1126/science.1207824>, 2011.

1128 Bond, T. C., Streets, D. G., Yarber, K. F., Nelson, S. M., Woo, J.-H., and Klimont, Z.: A technology-based global inventory
1129 of black and organic carbon emissions from combustion, <https://doi.org/10.1029/2003JD003697>, 2004.

1130 Bond, T. C., Bhardwaj, E., Dong, R., Jogani, R., Jung, S., Roden, C., Streets, D. G., and Trautmann, N. M.: Historical emissions
1131 of black and organic carbon aerosol from energy-related combustion, 1850–2000, *Global Biogeochemical Cycles*, 21,
1132 <https://doi.org/10.1029/2006GB002840>, 2007.

1133 Chen, F. and Chen, Z.: Cost of economic growth: Air pollution and health expenditure, *Science of The Total Environment*,
1134 755, 142543, <https://doi.org/10.1016/j.scitotenv.2020.142543>, 2021.

1135 Cho, C., Franchin, A., Flocke, F., Lesko, K., Owen, C., Hall, S. R., Ullmann, K., Apel, E. C., Hills, A. J., Hornbrook, R. S.,
1136 Roozitalab, B., Jeong, D., Diskin, G. S., Choi, Y., DiGangi, J. P., Miech, J., Wolfe, G. M., Hanisco, T. F., St. Clair, J. M.,
1137 Liao, J., Delaria, E. R., Sebol, A., Hannun, R. A., Wennberg, P. O., Ball, K., Lee, Y. R., Huey, L. G., Tanner, D. J., Arterburn,
1138 L., Blake, D. R., Blake, N. J., Barletta, B., Meinardi, S., Min, K.-E., Kang, H., Nam, W., Wisthaler, A., Piel, F., Wojnowski,
1139 W., Dibb, J., and Crawford, J.: Insights on Ozone Formation Sensitivity in Southeast and East Asian Megacities during ASIA-
1140 AQ, *EGUsphere*, 1–29, <https://doi.org/10.5194/egusphere-2025-6434>, 2026.

1141 Choi, S., Lamsal, L. N., Follette-Cook, M., Joiner, J., Krotkov, N. A., Swartz, W. H., Pickering, K. E., Loughner, C. P., Appel,
1142 W., Pfister, G., Saide, P. E., Cohen, R. C., Weinheimer, A. J., and Herman, J. R.: Assessment of NO₂ observations during
1143 DISCOVER-AQ and KORUS-AQ field campaigns, *Atmospheric Measurement Techniques*, 13, 2523–2546,
1144 <https://doi.org/10.5194/amt-13-2523-2020>, 2020.

1145 Christopoulos, J. A., Saide, P. E., Ferrare, R., Collister, B., Barton-Grimley, R. A., Scarino, A. J., Collins, J., Hair, J. W., and
1146 Nehrir, A.: Improving Planetary Boundary Layer Height Estimation From Airborne Lidar Instruments, *Journal of Geophysical*
1147 *Research: Atmospheres*, 130, e2024JD042538, <https://doi.org/10.1029/2024JD042538>, 2025.

1148 Christopoulos, J.: GEMS Top-Down NO_x Emissions and Model Optimization, Zenodo,
1149 <https://doi.org/10.5281/zenodo.18381169>, 2026.

1150

1151 Commerce, N. C. for E. P. W. S. S. D. of: NCEP FNL Operational Model Global Tropospheric Analyses, continuing from
1152 July 1999, <https://doi.org/10.5065/D6M043C6>, 2000.

1153 Crippa, M., Solazzo, E., Huang, G., Guizzardi, D., Koffi, E., Muntean, M., Schieberle, C., Friedrich, R., and Janssens-
1154 Maenhout, G.: High resolution temporal profiles in the Emissions Database for Global Atmospheric Research, *Sci Data*, 7,
1155 121, <https://doi.org/10.1038/s41597-020-0462-2>, 2020.

1156 Elguindi, N., Granier, C., Stavrakou, T., Darras, S., Bauwens, M., Cao, H., Chen, C., Denier van der Gon, H. a. C., Dubovik,
1157 O., Fu, T. M., Henze, D. K., Jiang, Z., Keita, S., Kuenen, J. J. P., Kurokawa, J., Liousse, C., Miyazaki, K., Müller, J.-F., Qu,
1158 Z., Solmon, F., and Zheng, B.: Intercomparison of Magnitudes and Trends in Anthropogenic Surface Emissions From Bottom-
1159 Up Inventories, Top-Down Estimates, and Emission Scenarios, *Earth’s Future*, 8, e2020EF001520,
1160 <https://doi.org/10.1029/2020EF001520>, 2020.

1161 de Foy, B. and Schauer, J. J.: An improved understanding of NO_x emissions in South Asian megacities using TROPOMI NO₂
1162 retrievals, *Environ. Res. Lett.*, 17, 024006, <https://doi.org/10.1088/1748-9326/ac48b4>, 2022.

- 1163 Fuller, R., Landrigan, P. J., Balakrishnan, K., Bathan, G., Bose-O'Reilly, S., Brauer, M., Caravanos, J., Chiles, T., Cohen, A.,
1164 Corra, L., Cropper, M., Ferraro, G., Hanna, J., Hanrahan, D., Hu, H., Hunter, D., Janata, G., Kupka, R., Lanphear, B., Lichtveld,
1165 M., Martin, K., Mustapha, A., Sanchez-Triana, E., Sandilya, K., Schaeffli, L., Shaw, J., Seddon, J., Suk, W., Téllez-Rojo, M.
1166 M., and Yan, C.: Pollution and health: a progress update, *The Lancet Planetary Health*, 6, e535–e547,
1167 [https://doi.org/10.1016/S2542-5196\(22\)00090-0](https://doi.org/10.1016/S2542-5196(22)00090-0), 2022.
- 1168 Gao, Z. and Zhou, X.: A review of the CAMx, CMAQ, WRF-Chem and NAQPMS models: Application, evaluation and
1169 uncertainty factors, *Environmental Pollution*, 343, 123183, <https://doi.org/10.1016/j.envpol.2023.123183>, 2024.
- 1170 Georgoulias, A. K., van der A, R. J., Stammes, P., Boersma, K. F., and Eskes, H. J.: Trends and trend reversal detection in 2
1171 decades of tropospheric NO₂ satellite observations, *Atmospheric Chemistry and Physics*, 19, 6269–6294,
1172 <https://doi.org/10.5194/acp-19-6269-2019>, 2019.
- 1173 Goldberg, D. L., Lamsal, L. N., Loughner, C. P., Swartz, W. H., Lu, Z., and Streets, D. G.: A high-resolution and
1174 observationally constrained OMI NO₂ satellite retrieval, *Atmospheric Chemistry and Physics*, 17, 11403–11421,
1175 <https://doi.org/10.5194/acp-17-11403-2017>, 2017.
- 1176 Goldberg, D. L., Saide, P. E., Lamsal, L. N., de Foy, B., Lu, Z., Woo, J.-H., Kim, Y., Kim, J., Gao, M., Carmichael, G., and
1177 Streets, D. G.: A top-down assessment using OMI NO₂ suggests an underestimate in the NO_x emissions inventory in Seoul,
1178 South Korea, during KORUS-AQ, *Atmospheric Chemistry and Physics*, 19, 1801–1818, [https://doi.org/10.5194/acp-19-1801-](https://doi.org/10.5194/acp-19-1801-2019)
1179 2019, 2019.
- 1180 Goldberg, D. L., Tao, M., Kerr, G. H., Ma, S., Tong, D. Q., Fiore, A. M., Dickens, A. F., Adelman, Z. E., and Anenberg, S.
1181 C.: Evaluating the spatial patterns of U.S. urban NO_x emissions using TROPOMI NO₂, *Remote Sensing of Environment*, 300,
1182 113917, <https://doi.org/10.1016/j.rse.2023.113917>, 2024.
- 1183 Gong, S. L., Barrie, L. A., and Blanchet, J.-P.: Modeling sea-salt aerosols in the atmosphere: 1. Model development, *Journal*
1184 *of Geophysical Research: Atmospheres*, 102, 3805–3818, <https://doi.org/10.1029/96JD02953>, 1997.
- 1185 Graziosi, F. and Manca, G.: Quantification of Hotspot Methane Emissions Using Sentinel-5P TROPOMI Observations, JRC
1186 Publications Repository, <https://doi.org/10.2760/4473858>, 2025.
- 1187 Grell, G., Freitas, S. R., Stuefer, M., and Fast, J.: Inclusion of biomass burning in WRF-Chem: impact of wildfires on weather
1188 forecasts, *Atmospheric Chemistry and Physics*, 11, 5289–5303, <https://doi.org/10.5194/acp-11-5289-2011>, 2011.

1189 Guenther, A., Karl, T., Harley, P., Wiedinmyer, C., Palmer, P. I., and Geron, C.: Estimates of global terrestrial isoprene
1190 emissions using MEGAN (Model of Emissions of Gases and Aerosols from Nature), *Atmospheric Chemistry and Physics*, 6,
1191 3181–3210, <https://doi.org/10.5194/acp-6-3181-2006>, 2006.

1192 Guizzardi, D., Crippa, M., Butler, T., Keating, T., Wu, R., Kaminski, J., Kuenen, J., Kurokawa, J., Chatani, S., Morikawa, T.,
1193 Pouliot, G., Racine, J., Moran, M. D., Klimont, Z., Manseau, P. M., Mashayekhi, R., Henderson, B. H., Smith, S. J., Hoesly,
1194 R., Muntean, M., Banja, M., Schaaf, E., Pagani, F., Woo, J.-H., Kim, J., Pisoni, E., Zhang, J., Niemi, D., Sassi, M., Duhamel,
1195 A., Ansari, T., Foley, K., Geng, G., Chen, Y., and Zhang, Q.: The HTAP_v3.2 emission mosaic: merging regional and global
1196 monthly emissions (2000–2020) to support air quality modelling and policies, *Earth System Science Data*, 17, 5915–5950,
1197 <https://doi.org/10.5194/essd-17-5915-2025>, 2025.

1198 Gulde, S. T., Kolm, M. G., Smith, D. J., Maurer, R., Courrèges-Lacoste, G. B., Sallusti, M., and Bagnasco, G.: Sentinel 4: a
1199 geostationary imaging UVN spectrometer for air quality monitoring: status of design, performance and development, in:
1200 International Conference on Space Optics — ICSO 2014, International Conference on Space Optics — ICSO 2014, 1158–
1201 1166, <https://doi.org/10.1117/12.2304099>, 2017.

1202 Hakkarainen, J., Nurmela, J., and Lindqvist, H.: D4.4 Benchmarking of plume detection and quantification methods, 2023.

1203 Hakkarainen, J., Kuhlmann, G., Koene, E., Santaren, D., Meier, S., Krol, M. C., van Stratum, B. J. H., Ialongo, I., Chevallier,
1204 F., Tamminen, J., Brunner, D., and Broquet, G.: Analyzing nitrogen dioxide to nitrogen oxide scaling factors for data-driven
1205 satellite-based emission estimation methods: A case study of Matimba/Medupi power stations in South Africa, *Atmospheric*
1206 *Pollution Research*, 15, 102171, <https://doi.org/10.1016/j.apr.2024.102171>, 2024.

1207 Hoesly, R. M., Smith, S. J., Feng, L., Klimont, Z., Janssens-Maenhout, G., Pitkanen, T., Seibert, J. J., Vu, L., Andres, R. J.,
1208 Bolt, R. M., Bond, T. C., Dawidowski, L., Kholod, N., Kurokawa, J., Li, M., Liu, L., Lu, Z., Moura, M. C. P., O'Rourke, P.
1209 R., and Zhang, Q.: Historical (1750–2014) anthropogenic emissions of reactive gases and aerosols from the Community
1210 Emissions Data System (CEDS), *Geoscientific Model Development*, 11, 369–408, <https://doi.org/10.5194/gmd-11-369-2018>,
1211 2018.

1212 Hsu, C.-H., Henze, D. K., Mizzi, A. P., Harkins, C., Lyu, C., Cooper, O. R., Schwantes, R. H., He, J., Li, M., Wang, S.,
1213 Stockwell, C. E., Warneke, C., Rollins, A. W., Waxman, E. M., Zuraski, K., Peischl, J., Kondragunta, S., Li, F., Xu, C., Pierce,
1214 R. B., Abad, G. G., Nowlan, C. R., Liu, X., and McDonald, B. C.: Top-Down Estimates of U.S. NO_x Emissions Using TEMPO
1215 and TROPOMI NO₂ Remote Sensing Observations With WRF-Chem/Chem-DART, *Journal of Geophysical Research:*
1216 *Atmospheres*, 131, e2025JD044223, <https://doi.org/10.1029/2025JD044223>, 2026.

1217 Inness, A., Ades, M., Agustí-Panareda, A., Barré, J., Benedictow, A., Blechschmidt, A.-M., Dominguez, J. J., Engelen, R.,
1218 Eskes, H., Flemming, J., Huijnen, V., Jones, L., Kipling, Z., Massart, S., Parrington, M., Peuch, V.-H., Razinger, M., Remy,
1219 S., Schulz, M., and Suttie, M.: The CAMS reanalysis of atmospheric composition, *Atmospheric Chemistry and Physics*, 19,
1220 3515–3556, <https://doi.org/10.5194/acp-19-3515-2019>, 2019.

1221 Janz, S. J., Kowalewski, M., Lamsal, L., Nowlan, C., and Judd, L.: Airborne hyperspectral trace gas sensors as testbeds for
1222 geostationary air quality missions, in: *Sensors, Systems, and Next-Generation Satellites XXIII*, *Sensors, Systems, and Next-*
1223 *Generation Satellites XXIII*, 509–518, <https://doi.org/10.1117/12.2533765>, 2019.

1224 Jiawei Zhuang, raphael dussin, David Huard, Pascal Bourgault, Anderson Banahirwe, Stephane Raynaud, Brewster Malevich,
1225 Martin Schupfner, Filipe, Charles Gauthier, Sam Levang, André Jüling, Mattia Almansì, RichardScottOZ, RondeauG, Stephan
1226 Rasp, Trevor James Smith, Ben Mares, Jemma Stachelek, Matthew Plough, Pierre, Ray Bell, Romain Caneill, and Xianxiang
1227 Li: *pangeo-data/xESMF: v0.8.10*, , <https://doi.org/10.5281/ZENODO.4294774>, 2025.

1228 Judd, L. M., Al-Saadi, J. A., Szykman, J. J., Valin, L. C., Janz, S. J., Kowalewski, M. G., Eskes, H. J., Veefkind, J. P., Cede,
1229 A., Mueller, M., Gebetsberger, M., Swap, R., Pierce, R. B., Nowlan, C. R., Abad, G. G., Nehrir, A., and Williams, D.:
1230 Evaluating Sentinel-5P TROPOMI tropospheric NO₂ column densities with airborne and Pandora spectrometers near New
1231 York City and Long Island Sound, *Atmospheric Measurement Techniques*, 13, 6113–6140, [https://doi.org/10.5194/amt-13-](https://doi.org/10.5194/amt-13-6113-2020)
1232 [6113-2020](https://doi.org/10.5194/amt-13-6113-2020), 2020.

1233 Jung, Y., Park, J., Hong, H., Lee, H., and Jeong, U.: Evaluation of GEMS NO Retrieval Algorithm Version 2.0 and 3.0 Using
1234 TROPOMI and Pandora Observations, *Korean Journal of Remote Sensing*, 41, 803–811,
1235 <https://doi.org/10.7780/kjrs.2025.41.5.8>, 2025.

1236 Kim, J., Jeong, U., Ahn, M.-H., Kim, J. H., Park, R. J., Lee, H., Song, C. H., Choi, Y.-S., Lee, K.-H., Yoo, J.-M., Jeong, M.-
1237 J., Park, S. K., Lee, K.-M., Song, C.-K., Kim, S.-W., Kim, Y. J., Kim, S.-W., Kim, M., Go, S., Liu, X., Chance, K., Miller, C.
1238 C., Al-Saadi, J., Veihelmann, B., Bhartia, P. K., Torres, O., Abad, G. G., Haffner, D. P., Ko, D. H., Lee, S. H., Woo, J.-H.,
1239 Chong, H., Park, S. S., Nicks, D., Choi, W. J., Moon, K.-J., Cho, A., Yoon, J., Kim, S., Hong, H., Lee, K., Lee, H., Lee, S.,
1240 Choi, M., Veefkind, P., Levelt, P. F., Edwards, D. P., Kang, M., Eo, M., Bak, J., Baek, K., Kwon, H.-A., Yang, J., Park, J.,
1241 Han, K. M., Kim, B.-R., Shin, H.-W., Choi, H., Lee, E., Chong, J., Cha, Y., Koo, J.-H., Irie, H., Hayashida, S., Kasai, Y.,
1242 Kanaya, Y., Liu, C., Lin, J., Crawford, J. H., Carmichael, G. R., Newchurch, M. J., Lefter, B. L., Herman, J. R., Swap, R. J.,
1243 Lau, A. K. H., Kurosu, T. P., Jaross, G., Ahlers, B., Dobber, M., McElroy, C. T., and Choi, Y.: New Era of Air Quality
1244 Monitoring from Space: Geostationary Environment Monitoring Spectrometer (GEMS), [https://doi.org/10.1175/BAMS-D-18-](https://doi.org/10.1175/BAMS-D-18-0013.1)
1245 [0013.1](https://doi.org/10.1175/BAMS-D-18-0013.1), 2020.

1246 Koster, R. D., Darmenov, A. S., and da Silva, A. M.: The Quick Fire Emissions Dataset (QFED): Documentation of Versions
1247 2.1, 2.2 and 2.4: Technical Report Series on Global Modeling and Data Assimilation - Volume 38, 2015.

1248 Kowalewski, M. G. and Janz, S. J.: Remote sensing capabilities of the GeoCAPE Airborne Simulator, in: Earth Observing
1249 Systems XIX, Earth Observing Systems XIX, 496–507, <https://doi.org/10.1117/12.2062058>, 2014.

1250 Kuhlmann, G., Koene, E., Meier, S., Santaren, D., Broquet, G., Chevallier, F., Hakkarainen, J., Nurmela, J., Amorós, L.,
1251 Tamminen, J., and Brunner, D.: The *ddeg* Python library for point source quantification from remote sensing images (version
1252 1.0), Geoscientific Model Development, 17, 4773–4789, <https://doi.org/10.5194/gmd-17-4773-2024>, 2024.

1253 Kumar, R., Naja, M., Pfister, G. G., Barth, M. C., Wiedinmyer, C., and Brasseur, G. P.: Simulations over South Asia using the
1254 Weather Research and Forecasting model with Chemistry (WRF-Chem): chemistry evaluation and initial results, Geoscientific
1255 Model Development, 5, 619–648, <https://doi.org/10.5194/gmd-5-619-2012>, 2012.

1256 Kurokawa, J. and Ohara, T.: Long-term historical trends in air pollutant emissions in Asia: Regional Emission inventory in
1257 ASia (REAS) version 3, Atmospheric Chemistry and Physics, 20, 12761–12793, <https://doi.org/10.5194/acp-20-12761-2020>,
1258 2020.

1259 Lee, S., Bae, K., Janz, S. J., Judd, L. M., Xiong, S., Boehmler, J., Jung, Y., Lee, H.-J., Hong, H., Chang, L.-S., Kang, M., Ahn,
1260 M.-H., Song, C.-K., and Park, S. S.: Sensitivity analysis of NO₂ differential slant column density according to spatial resolution
1261 using GCAS data from the SIJAQ 2022 campaign, Atmospheric Environment, 335, 120723,
1262 <https://doi.org/10.1016/j.atmosenv.2024.120723>, 2024.

1263 Lennartson, E. M., Wang, J., Gu, J., Castro Garcia, L., Ge, C., Gao, M., Choi, M., Saide, P. E., Carmichael, G. R., Kim, J., and
1264 Janz, S. J.: Diurnal variation of aerosol optical depth and PM_{2.5} in South Korea: a synthesis from AERONET, satellite (GOCI),
1265 KORUS-AQ observation, and the WRF-Chem model, Atmospheric Chemistry and Physics, 18, 15125–15144,
1266 <https://doi.org/10.5194/acp-18-15125-2018>, 2018.

1267 Li, M., Kurokawa, J., Zhang, Q., Woo, J.-H., Morikawa, T., Chatani, S., Lu, Z., Song, Y., Geng, G., Hu, H., Kim, J., Cooper,
1268 O. R., and McDonald, B. C.: MIXv2: a long-term mosaic emission inventory for Asia (2010–2017), Atmospheric Chemistry
1269 and Physics, 24, 3925–3952, <https://doi.org/10.5194/acp-24-3925-2024>, 2024.

1270 Liu, J., Gao, H., Jia, R., Wang, R., Han, D., Liu, L., Xu, X., and Qiao, Z.: A downscaling framework with WRF-UCM and
1271 LES/RANS models for urban microclimate simulation strategy: Validation through both measurement and mechanism model,
1272 Building and Environment, 269, 112361, <https://doi.org/10.1016/j.buildenv.2024.112361>, 2025.

- 1273 Makkwao, K. and Prueksasit, T.: PM10 Concentration Emitted from Blasting and Crushing Processes of Limestone Mines in
1274 Saraburi Province, Thailand, 2021.
- 1275 Meier, S., Koene, E. F. M., Krol, M., Brunner, D., Damm, A., and Kuhlmann, G.: A lightweight NO₂-to-NO_x conversion model
1276 for quantifying NO_x emissions of point sources from NO₂ satellite observations, *Atmospheric Chemistry and Physics*, 24,
1277 7667–7686, <https://doi.org/10.5194/acp-24-7667-2024>, 2024.
- 1278 Miyazaki, K., Eskes, H., Sudo, K., Boersma, K. F., Bowman, K., and Kanaya, Y.: Decadal changes in global surface NO_x
1279 emissions from multi-constituent satellite data assimilation, *Atmospheric Chemistry and Physics*, 17, 807–837,
1280 <https://doi.org/10.5194/acp-17-807-2017>, 2017.
- 1281 Miyazaki, K., Sekiya, T., Fu, D., Bowman, K. W., Kulawik, S. S., Sudo, K., Walker, T., Kanaya, Y., Takigawa, M., Ogochi,
1282 K., Eskes, H., Boersma, K. F., Thompson, A. M., Gaubert, B., Barre, J., and Emmons, L. K.: Balance of Emission and
1283 Dynamical Controls on Ozone During the Korea-United States Air Quality Campaign From Multiconstituent Satellite Data
1284 Assimilation, *Journal of Geophysical Research: Atmospheres*, 124, 387–413, <https://doi.org/10.1029/2018JD028912>, 2019.
- 1285 Miyazaki, K., Bowman, K., Sekiya, T., Eskes, H., Boersma, F., Worden, H., Livesey, N., Payne, V. H., Sudo, K., Kanaya, Y.,
1286 Takigawa, M., and Ogochi, K.: Updated tropospheric chemistry reanalysis and emission estimates, TCR-2, for 2005–2018,
1287 *Earth System Science Data*, 12, 2223–2259, <https://doi.org/10.5194/essd-12-2223-2020>, 2020.
- 1288 Mues, A., Kuenen, J., Hendriks, C., Manders, A., Segers, A., Scholz, Y., Hueglin, C., Bultjes, P., and Schaap, M.: Sensitivity
1289 of air pollution simulations with LOTOS-EUROS to the temporal distribution of anthropogenic emissions, *Atmospheric
1290 Chemistry and Physics*, 14, 939–955, <https://doi.org/10.5194/acp-14-939-2014>, 2014.
- 1291 Nocedal, J. and Wright, S. J.: *Numerical optimization*, 2nd ed., Springer, New York, 664 pp., 2006.
- 1292 Oda, T., Maksyutov, S., and Andres, R. J.: The Open-source Data Inventory for Anthropogenic CO₂ , version 2016
1293 (ODIAC2016): a global monthly fossil fuel CO₂ gridded emissions data product for tracer transport simulations and surface
1294 flux inversions, *Earth Syst. Sci. Data*, 10, 87–107, <https://doi.org/10.5194/essd-10-87-2018>, 2018.
- 1295 Park, J., Choi, Y., Jung, J., Lee, K., and Yeganeh, A. K.: First top-down diurnal adjustment to NO_x emissions inventory in
1296 Asia informed by the Geostationary Environment Monitoring Spectrometer (GEMS) tropospheric NO₂ columns, *Sci Rep*, 14,
1297 24338, <https://doi.org/10.1038/s41598-024-76223-1>, 2024.
- 1298 Park, J., Hong, H., Lee, H., Kim, S.-W., Kim, J., Van Roozendaal, M., Fayt, C., Ahn, M.-H., Jacob, D. J., Seo, S., Kim, K.-
1299 M., Kim, D., Choi, W., Lee, W.-J., Lee, D.-W., Wagner, T., Richter, A., Krotkov, N. A., Lamsal, L. N., Ko, D. H., Lee, S. H.,

1300 and Woo, J.-H.: Tropospheric nitrogen dioxide levels vary diurnally in Asian cities, *Commun Earth Environ*, 6, 389,
1301 <https://doi.org/10.1038/s43247-025-02272-7>, 2025.

1302 Park, R. J., Oak, Y. J., Emmons, L. K., Kim, C.-H., Pfister, G. G., Carmichael, G. R., Saide, P. E., Cho, S.-Y., Kim, S., Woo,
1303 J.-H., Crawford, J. H., Gaubert, B., Lee, H.-J., Park, S.-Y., Jo, Y.-J., Gao, M., Tang, B., Stanier, C. O., Shin, S. S., Park, H.
1304 Y., Bae, C., and Kim, E.: Multi-model intercomparisons of air quality simulations for the KORUS-AQ campaign, *Elementa:
1305 Science of the Anthropocene*, 9, 00139, <https://doi.org/10.1525/elementa.2021.00139>, 2021.

1306 Pörtner, H.-O., Roberts, D. C., Tignor, M. M. B., Poloczanska, E. S., Mintenbeck, K., Alegría, A., Craig, M., Langsdorf, S.,
1307 Löschke, S., Möller, V., Okem, A., and Rama, B. (Eds.): *Climate Change 2022: Impacts, Adaptation and Vulnerability.
1308 Contribution of Working Group II to the Sixth Assessment Report of the Intergovernmental Panel on Climate Change.*, 2022.

1309 Rey-Pommier, A., Héraud, A., Chevallier, F., Ciais, P., Christoudias, T., Kushta, J., and Sciare, J.: Global gridded NO_x
1310 emissions using TROPOMI observations, *Earth System Science Data*, 17, 3329–3351, [https://doi.org/10.5194/essd-17-3329-
1311 2025](https://doi.org/10.5194/essd-17-3329-2025), 2025.

1312 Ridley, B. A. and Grahek, F. E.: A Small, Low Flow, High Sensitivity Reaction Vessel for NO Chemiluminescence Detectors,
1313 1990.

1314 Ridley, B. A., Grahek, F. E., and Walega, J. G.: A Small High-Sensitivity, Medium-Response Ozone Detector Suitable for
1315 Measurements from Light Aircraft, 1992.

1316 Saide, P. E., Gao, M., Lu, Z., Goldberg, D. L., Streets, D. G., Woo, J.-H., Beyersdorf, A., Corr, C. A., Thornhill, K. L.,
1317 Anderson, B., Hair, J. W., Nehrir, A. R., Diskin, G. S., Jimenez, J. L., Nault, B. A., Campuzano-Jost, P., Dibb, J., Heim, E.,
1318 Lamb, K. D., Schwarz, J. P., Perring, A. E., Kim, J., Choi, M., Holben, B., Pfister, G., Hodzic, A., Carmichael, G. R., Emmons,
1319 L., and Crawford, J. H.: Understanding and improving model representation of aerosol optical properties for a Chinese haze
1320 event measured during KORUS-AQ, *Atmospheric Chemistry and Physics*, 20, 6455–6478, [https://doi.org/10.5194/acp-20-
1321 6455-2020](https://doi.org/10.5194/acp-20-6455-2020), 2020.

1322 Santaren, D., Hakkarainen, J., Kuhlmann, G., Koene, E., Chevallier, F., Ialongo, I., Lindqvist, H., Nurmela, J., Tamminen, J.,
1323 Amorós, L., Brunner, D., and Broquet, G.: Benchmarking data-driven inversion methods for the estimation of local CO₂
1324 emissions from synthetic satellite images of XCO₂ and NO₂, *Atmospheric Measurement Techniques*, 18, 211–239,
1325 <https://doi.org/10.5194/amt-18-211-2025>, 2025.

1326 Seinfeld and Pandis: *Atmospheric Chemistry and Physics: From Air Pollution to Climate Change*, 3rd Edition | Wiley, 2016.

- 1327 Shetty, S. S., D, D., S, H., Sonkusare, S., Naik, P. B., N, S. K., and Madhyastha, H.: Environmental pollutants and their effects
1328 on human health, *Heliyon*, 9, <https://doi.org/10.1016/j.heliyon.2023.e19496>, 2023.
- 1329 Sicard, P., Agathokleous, E., Anenberg, S. C., De Marco, A., Paoletti, E., and Calatayud, V.: Trends in urban air pollution
1330 over the last two decades: A global perspective, *Science of The Total Environment*, 858, 160064,
1331 <https://doi.org/10.1016/j.scitotenv.2022.160064>, 2023.
- 1332 Skamarock, W. C., Klemp, J. B., Dudhia, J., Gill, D. O., Liu, Z., Berner, J., Wang, W., Powers, J. G., Duda, M. G., Barker, D.
1333 M., and Huang, X.-Y.: A Description of the Advanced Research WRF Model Version 4, <https://doi.org/10.5065/1DFH-6P97>,
1334 2019.
- 1335 Smith, S. J., van Aardenne, J., Klimont, Z., Andres, R. J., Volke, A., and Delgado Arias, S.: Anthropogenic sulfur dioxide
1336 emissions: 1850–2005, *Atmospheric Chemistry and Physics*, 11, 1101–1116, <https://doi.org/10.5194/acp-11-1101-2011>, 2011.
- 1337 St. Clair, J. M., Swanson, A. K., Bailey, S. A., and Hanisco, T. F.: CAFE: a new, improved nonresonant laser-induced
1338 fluorescence instrument for airborne in situ measurement of formaldehyde, *Atmospheric Measurement Techniques*, 12, 4581–
1339 4590, <https://doi.org/10.5194/amt-12-4581-2019>, 2019.
- 1340 Thailand Office of the National Economic and Social Development Board, World Bank: Industrial Change in the Bangkok
1341 Urban Region, 2017.
- 1342 Tuccella, P., Curci, G., Grell, G. A., Visconti, G., Crumeyrolle, S., Schwarzenboeck, A., and Mensah, A. A.: A new chemistry
1343 option in WRF-Chem v. 3.4 for the simulation of direct and indirect aerosol effects using VBS: evaluation against IMPACT-
1344 EUCAARI data, *Geoscientific Model Development*, 8, 2749–2776, <https://doi.org/10.5194/gmd-8-2749-2015>, 2015.
- 1345 Uttamang, P., Aneja, V. P., and Hanna, A. F.: Assessment of gaseous criteria pollutants in the Bangkok Metropolitan Region,
1346 Thailand, *Atmospheric Chemistry and Physics*, 18, 12581–12593, <https://doi.org/10.5194/acp-18-12581-2018>, 2018.
- 1347 Uttamang, P., Campbell, P. C., Aneja, V. P., and Hanna, A. F.: A multi-scale model analysis of ozone formation in the Bangkok
1348 Metropolitan Region, Thailand, *Atmospheric Environment*, 229, 117433, <https://doi.org/10.1016/j.atmosenv.2020.117433>,
1349 2020.
- 1350 Uttamang, P., Choomanee, P., Phupijit, J., Bualert, S., and Thongyen, T.: Investigation of Secondary Organic Aerosol
1351 Formation during O₃ and PM_{2.5} Episodes in Bangkok, Thailand, *Atmosphere*, 14, 994,
1352 <https://doi.org/10.3390/atmos14060994>, 2023.

1353 Valin, L. C., Russell, A. R., Hudman, R. C., and Cohen, R. C.: Effects of model resolution on the interpretation of satellite
1354 NO₂ observations, *Atmospheric Chemistry and Physics*, 11, 11647–11655, <https://doi.org/10.5194/acp-11-11647-2011>, 2011.

1355 Verreyken, B. W. D., Harkins, C., Li, M., Angevine, W., Stockwell, C. E., Xu, L., Coggon, M., Gilman, J., Warneke, C.,
1356 Strobach, E., Brown, S., McCarty, B., Marchbanks, R., Baidar, S., Brewer, A., Pfannerstill, E. Y., Arata, C., Goldstein, A. H.,
1357 Brioude, J., and McDonald, B. C.: Top-Down Evaluation of Volatile Chemical Product Emissions Using a Lagrangian
1358 Framework, *Environ. Sci. Technol.*, 59, 7211–7221, <https://doi.org/10.1021/acs.est.4c10117>, 2025.

1359 Ye, J., Liu, L., Wang, Q., Hu, S., and Li, S.: A Novel Machine Learning Algorithm for Planetary Boundary Layer Height
1360 Estimation Using AERI Measurement Data, *IEEE Geoscience and Remote Sensing Letters*, 19,
1361 <https://doi.org/10.1109/lgrs.2021.3073048>, 2021.

1362 Yu, K. A., Li, M., Harkins, C., He, J., Zhu, Q., Verreyken, B., Schwantes, R. H., Cohen, R. C., McDonald, B. C., and Harley,
1363 R. A.: Improved Spatial Resolution in Modeling of Nitrogen Oxide Concentrations in the Los Angeles Basin, *Environ. Sci.*
1364 *Technol.*, 57, 20689–20698, <https://doi.org/10.1021/acs.est.3c06158>, 2023.

1365 Zhao, C., Liu, X., Leung, L. R., Johnson, B., McFarlane, S. A., Gustafson, W. I. J., Fast, J. D., and Easter, R.: The spatial
1366 distribution of mineral dust and its shortwave radiative forcing over North Africa: modeling sensitivities to dust emissions and
1367 aerosol size treatments, *Atmospheric Chemistry and Physics*, 10, 8821–8838, <https://doi.org/10.5194/acp-10-8821-2010>, 2010.

1368 Zoogman, P., Liu, X., Suleiman, R. M., Pennington, W. F., Flittner, D. E., Al-Saadi, J. A., Hilton, B. B., Nicks, D. K.,
1369 Newchurch, M. J., Carr, J. L., Janz, S. J., Andraschko, M. R., Arola, A., Baker, B. D., Canova, B. P., Chan Miller, C., Cohen,
1370 R. C., Davis, J. E., Dussault, M. E., Edwards, D. P., Fishman, J., Ghulam, A., González Abad, G., Grutter, M., Herman, J. R.,
1371 Houck, J., Jacob, D. J., Joiner, J., Kerridge, B. J., Kim, J., Krotkov, N. A., Lamsal, L., Li, C., Lindfors, A., Martin, R. V.,
1372 McElroy, C. T., McLinden, C., Natraj, V., Neil, D. O., Nowlan, C. R., O’Sullivan, E. J., Palmer, P. I., Pierce, R. B., Pippin, M.
1373 R., Saiz-Lopez, A., Spurr, R. J. D., Szykman, J. J., Torres, O., Veefkind, J. P., Veihelmann, B., Wang, H., Wang, J., and
1374 Chance, K.: Tropospheric emissions: Monitoring of pollution (TEMPO), *Journal of Quantitative Spectroscopy and Radiative*
1375 *Transfer*, 186, 17–39, <https://doi.org/10.1016/j.jqsrt.2016.05.008>, 2017.

1376

1377

1378

1379

1380